

Revisiting Image Deblurring with an Efficient ConvNet

Lingyan Ruan Mojtaba Bermana Hans-peter Seidel Karol Myszkowski Bin Chen*

Max-Planck-Institut für Informatik

<https://github.com/lingyanruan/LaKDNet>

Abstract

Image deblurring aims to recover the latent sharp image from its blurry counterpart and has a wide range of applications in computer vision. The Convolution Neural Networks (CNNs) have performed well in this domain for many years, and until recently an alternative network architecture, namely Transformer, has demonstrated even stronger performance. One can attribute its superiority to the multi-head self-attention (MHSA) mechanism, which offers a larger receptive field and better input content adaptability than CNNs. However, as MHSA demands high computational costs that grow quadratically with respect to the input resolution, it becomes impractical for high-resolution image deblurring tasks. In this work, we propose a unified lightweight CNN network that features a large effective receptive field (ERF) and demonstrates comparable or even better performance than Transformers while bearing less computational costs. Our key design is an efficient CNN block dubbed LaKD, equipped with a large kernel depth-wise convolution and spatial-channel mixing structure, attaining comparable or larger ERF than Transformers but with a smaller parameter scale. Specifically, we achieve +0.17dB / +0.43dB PSNR over the state-of-the-art Restormer on defocus / motion deblurring benchmark datasets with 32% fewer parameters and 39% fewer MACs. Extensive experiments demonstrate the superior performance of our network and the effectiveness of each module. Furthermore, we propose a compact and intuitive ERFMeter metric that quantitatively characterizes ERF, and shows a high correlation to the network performance. We hope this work can inspire the research community to further explore the pros and cons of CNN and Transformer architectures beyond image deblurring tasks.

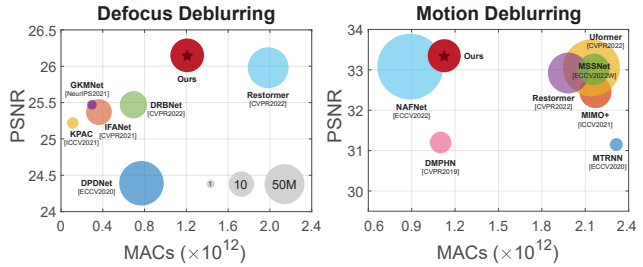


Figure 1. Motion and defocus deblurring results (PSNR) vs. parameters (M, disk size) vs. computational cost (MACs). Our method achieves the SOTA performance while maintaining efficiency.

1. Introduction

Image deblurring plays a major role in the low-level vision realm, especially in the digital age where the camera, as one of the essential parts, has been integrated into almost all types of personal electronic devices. Recovering the latent sharp image from its blurred counterpart has immediate applications on consumer-level electronics and potential benefits to a wide range of vision tasks like object detection [50], image classification [33], text recognition [42], as well as surveillance [67] and autonomous driving systems [20]. Traditional algorithms depend on blur kernel estimation and blind deconvolution with priors or regularizers to restore sharp images from the observed blurry version [55]. Even though significant progress has been made, the deblurring performance is still limited and tends to introduce unwanted artifacts [83]. In the last two decades, CNNs have become a promising tool for image deblurring tasks. Given a large dataset, CNNs have the ability to learn the corresponding priors, which then can be used for image deblurring at inference [2, 11, 28, 32, 43, 53, 63, 85, 86], showing high efficiency and generalization ability [57]. While on the one hand, the inherent inductive biases contribute to the efficiency of the network; on the other hand, it limits the network’s ability to model long-range spatial dependencies.

Recently, Transformer, an alternative structure, appears to alleviate the constraints of CNN, and shows compelling

* denotes corresponding author.

performance on several tasks in natural language processing [4,5,16,72] and computer vision [6,19,69,82,90]. While the MHSA module in the Transformer solves the long-range spatial dependencies problem, it increases computational complexity. This situation worsens on high-resolution images, where the computational complexity grows quadratically. Although there have been some attempts to relieve the computational burden by bringing back the inductive bias of CNNs [14,37,71], the computational expense is still considerable. Until recently, Restormer [84], in contrast to [37,75], applied self-attention (SA) across the feature dimension instead of the spatial dimension, reducing the computational loads to some extent. Nevertheless, all the Transformer-based approaches benefit from the MHSA mechanism, which is believed to be mainly responsible for creating the large receptive field [49]. A question naturally raises: is it possible to design a pure CNN module capable of approaching a large receptive field with comparable performance to Transformers? Recent works [38,68,70] resort to the existing network structures, *e.g.* ResNet [22], or MobileNet V2 [55], with several modifications, such as group convolution [12], inverted bottleneck [55], or large kernel [17,36], demonstrating competitive performance on par with Transformers on a similar model scale. Particularly, RepLKNet [17] and SLaK [36] build pure CNN models with a focus on increasing ERF using kernel sizes as large as 31×31 and 51×51 , respectively. While they achieve comparable performance to the Transformer, such explorations of large kernel CNNs are limited to the image classification task. Unlike image classification, which tends to address images with relatively low resolution, image deblurring usually deals with high-resolution inputs, thus imposing further challenges on network architecture design. Whether increasing ERF or equipping CNNs with a large kernel size impacts image deblurring quality has yet to be determined. In this paper, we explore in depth the effect of ERF and large kernel convolution on image deblurring and devise a pure CNN architecture with a block called LaKD, consisting of a large kernel depth-wise convolution and a spatial-channel mixing mechanism. Moreover, to quantify ERF’s influence, we suggest an ERF evaluation method dubbed ERFMeter, presenting a close correlation to the network performance with Pearson correlation coefficient $r = 0.8$ when evaluating a large number of networks. Overall, our contributions can be summarized as follows:

- To the best of our knowledge, we are the first to investigate the ERF of existing U-Net shape works for motion and defocus deblurring and associate their network performance with the ERF. We then present a quantified metric of the ERF, suggesting a more intuitive way to interpret their relationship across different structures.
- We propose a pure CNN structure being able to reach a large ERF, outperforming transformer structure

(Restormer / Uformer) on high-resolution image deblurring at a small computational cost, specifically sparing up to 66.4% / 34.6% parameters and 47.5% / 43.3% MACs.

- Extensive experimental and ablation results demonstrate the effectiveness of our method on various benchmark datasets in terms of motion and defocus deblurring.

2. Related Work

Image Deblurring Image deblurring is a long-standing research issue aiming to recover the latent fine textures from its observed version being corrupted by motion [43] or defocus [2] blur. Conventional blind image deblurring algorithms often start with kernel estimation, followed by non-blind deconvolution algorithms [10,26,58,78]. However, these two-step strategies are less effective in terms of quality and computational cost due to the error propagation occurring in their iterative optimization procedure. Later, CNN-based methods predominate in the image deblurring task by offering end-to-end solutions [2,11,28,32,43,48,53,63,85,86], and efficiently achieving remarkable results, most of which are tailored to a specific type of blur - motion or defocus. Transformer-based structures (*e.g.* Uformer [75], Restormer [84]) demonstrate strong ability on various image restoration tasks, including motion and defocus deblurring. However, these unified structures require multi-head self-attention [72], resulting in a heavy computational load despite some efforts (*e.g.* narrow down the attention window [37,75] or divide the image into patches [8] for MHSA) to reduce the costs. In this paper, we explore a pure CNN structure, in contrast to SA, to attain competitive performance on par with or better than the Transformer on a much smaller computation budget.

Transformer The Transformer architecture first took the natural language processing (NLP) community [4,5,16,72] by storm. Later, Dosovitskiy et al. introduced *Vision Transformers (ViTs)*, allowing applications of Transformers on image data [19]. Since then, it has gained a dominant position in a very short time on a broad range of computer vision tasks [6,19,34,69,75,77,79,82,84,89,90]. Unlike the conventional CNN that has an inherent inductive bias to the local receptive field, Transformer architectures with a self-attention mechanism allow each pixel to interact with all other pixels in a given patch, yielding a global receptive field and long-range feature dependencies [72]. Moreover, the convolution filters in self-attention modules are estimated on-the-fly according to the input content, outperforming conventional CNNs, especially at the inference stage [27]. However, the intensive computational cost restricts applications of the Transformer on high-resolution image data. Thus giving way to the rising trend of new ar-

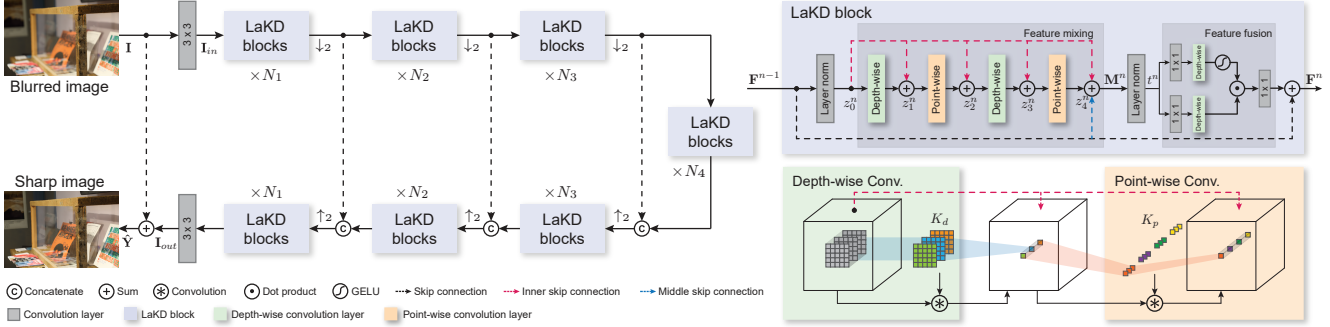


Figure 2. Our U-shape network architecture consists of 4-level symmetric encoder-decoder modules, with each level composed of N LaKD blocks. The LaKD block (top right) contains a feature mixing module and a feature fusion module, where the feature mixing module has depth-wise and point-wise convolution repeated twice, whereas the feature fusion module has only a depth-wise convolution layer with 3×3 kernel in a gating mechanism [15]. The details are better viewed when zooming in.

architectures that borrow useful properties from CNNs, and at the same time, avoid their shortcomings [37, 74, 81]. Swin Transformer [37] re-introduces the inductive bias of CNNs to Transformers using a sliding window in a hierarchical architecture to reduce the parameter count and computational cost. This structure has been successfully used as a general-purpose backbone on multiple computer vision tasks [34, 37, 64].

Large Kernels Following a similar spirit, some works explore the inverse approach, introducing the merits of Transformer to CNN. Attributing the superiority of ViTs to their large receptive field, researchers resorted back to pure CNNs equipped with larger kernels. This is a well-known older technique; some early works have used large kernel convolution neural networks [29] for image classification, such as 11×11 or 5×5 , but since the advent of VGG [62], they were overtaken by multiple stacked small kernels (3×3), which have fewer parameters and enable efficient training. Recent works, influenced by the global attention property of Transformers and MLPs, re-investigate the large convolutional kernels. ConvNeXt [38] adapts the existing ResNet architecture with 7×7 kernels, RepLKNet [17] and SLaKNet [36] scale up their kernels to 31×31 and 51×51 , both of which are purely convolutional neural networks, while achieving performance on par with or even better than Transformers [37] on image classification and a few downstream vision tasks. However, little effort has been made to explore the impact of large kernels in image restoration tasks. We investigate the ERF of existing works and propose a unified full CNN structure with large kernels aiming for a large ERF that achieves competitive performance while maintaining efficiency with much fewer parameters and lower computational cost.

3. Methodology

Our method aims to develop an efficient pure CNN model to restore sharp, high-resolution image \hat{Y} from their blurry version I . To maintain efficiency while attaining a

large ERF, we resort to depth-wise convolution with uncommonly large kernels, in contrast to self-attention, to model long-range pixel dependencies. In this section, we introduce the overall structure dubbed LaKNet and then provide the details of the proposed basic LaKD block.

3.1. Overall architecture

The overall architecture is a U-shape hierarchical network [52]. It consists of 4-level symmetric encoder-decoder modules, with each level composed of N LaKD blocks, where $N \in \{N_1, N_2, N_3, N_4\}$. Given an input image $I \in \mathbb{R}^{H \times W \times 3}$ with height (H) and width (W), our network first extracts low-level features $I_{in} \in \mathbb{R}^{H \times W \times C}$ with C channels using a convolutional layer. Then, it is fed into our encoder-decoder structure for blur removal, followed by another convolution layer to recover the features $I_{out} \in \mathbb{R}^{H \times W \times C}$. We apply pixel unshuffle/shuffle for downsampling and upsampling respectively [61, 84]. Finally, we skip-connect I to I_{out} and produce the sharp image \hat{Y} , forming a global residual structure that is expressed as $\hat{Y} = I + \text{LaKNet}(I)$.

3.2. LaKD Block

The motivation behind the LaKD block design is to explore the local and global dependency, as well as a large ERF, in a fully convolutional manner. It has two submodules – feature mixer and feature fusion indicated in Fig. 2. The feature mixer module is similar in spirit to depth-wise separable convolution, but at initial stages employs unusually large kernel sizes (e.g. 9×9) followed by point-wise convolution with a kernel size of 1×1 , along with the inner shortcut between them. Unlike the standard convolution layers, which mix spatial and channel dimensions simultaneously through 3D filters, our feature mixer acts separately on spatial intra-channel and depth-wise inter-channel features. This allows distant spatial location mixture, which combined with large kernel sizes, leads to large ERF (Sec. 4.2). Our design is inspired by MLP-mixer [68]

and ConvMixer [70] which also separately mix spatial and channel dimensions. The former advocates the significance of multi-layer perceptrons (MLPs) and the latter focuses on the effectiveness of patch embedding for vision tasks, while we aim for correlating the feature mixer module to the ERF and the restoration performance. Our feature fusion module consists of depth-wise convolution layers with 3×3 kernels for efficient local information encoding. Similar to [84], we employ the gating mechanism [15] that specifically adds an extra path followed by GELU activation function [23] as the gate, in order to effectively propagate and fuse features. We first introduce our feature mixing module that outputs the feature \mathbf{M}^n in the n th LaKD block as follows:

$$\mathbf{M}^n = \mathbf{F}^{n-1} + z_k^n, \quad (1)$$

where \mathbf{F}^{n-1} is the output of the feature fusion module in the $n - 1$ th LaKD block and $1 < n \leq N$. The intermediate feature z_k is recursively calculated as:

$$z_{k+1}^n = z_k^n + g(z_k^n), \quad g = \begin{cases} \text{depthwise,} & \text{if } k = 1, 3 \\ \text{pointwise,} & \text{if } k = 2, 4 \end{cases} \quad (2)$$

where the depthwise and pointwise notations represent the depth-wise and point-wise convolutions, respectively and $z_0^n = \text{LN}(\mathbf{F}^{n-1})$, where LN is a layer normalization as shown in Fig. 2.

Next, we formulate the output feature \mathbf{F}^n from our feature fusion process as:

$$\mathbf{F}^n = \mathbf{F}^{n-1} + \text{LN}\{\alpha[g(W_1(t^n))] \odot g(W_2(t^n))\}, \quad (3)$$

where $t^n = \text{LN}(\mathbf{M}^n)$, W_1 and W_2 are two separate 1×1 convolution layers which are then combined as shown in Fig. 2 using an element-wise multiplication denoted as \odot and followed by a GELU activation α . Here, g only applies depth-wise convolution with 3×3 kernel. Our network includes LaKD blocks distributed in a hierarchical manner, allowing a large ERF, and contributing significantly to the fine details restoration. Note that our design shares a similar U-Net structure with Uformer [75] and Restormer [84] but is composed of different specialized blocks. We ablate the effectiveness of each component in Sec. 4.2.

3.3. ERFMeter

In this section, we aim to quantify the influence of ERF. Previous works [17, 36] mainly focus on enlarging the size of the receptive field through structural re-parameterization [18] or sparse large kernel. We claim that the size of a receptive field is not the determining factor that accounts for the word “effective” while the shape of the receptive field pattern also matters. We specifically find that the distribution of an ERF can be represented by the Probability Density Function (PDF) of the Generalized Normal Distribution

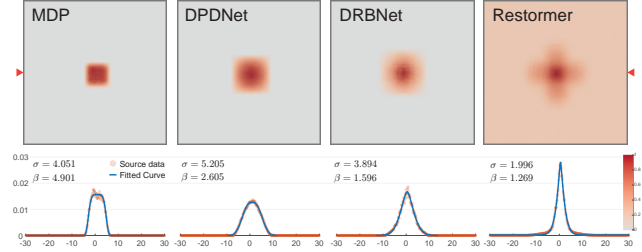


Figure 3. Demonstration of ERF patterns and the fitted GND-PDF curves. Note that, the ERF patterns are in log scale for better visualization, while the GND-PDF curves are in linear scale.

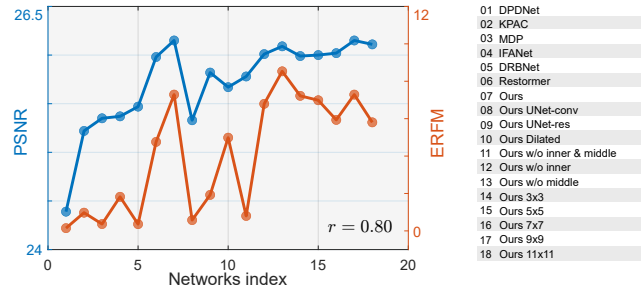


Figure 4. Correlation between ERFM and network performance. All networks were trained and tested on DPDD dataset. The Pearson Correlation Coefficient $r = 0.80$ between ERFM and PSNR of test networks.

(GND) family. Assuming that the averaged ERF pattern does not depend on the input content, we consider only a symmetric GND that can be derived as:

$$f(x) = \frac{c_1 \beta}{2\sigma \Gamma(1/\beta)} \exp\left(-\left|\frac{x - \mu}{\sigma}\right|^\beta\right) + c_2 \quad (4)$$

where x is the raw ERF values, $\mu \in \mathbb{R}$ represents the center of the distribution, and $\sigma \in \mathbb{R}_{>0}$ is the scaling factor that characterizes the variation of distribution: the larger σ indicates a more dispersed distribution. The parameter $\beta \in \mathbb{R}_{>0}$ controls the shape of the distribution, *e.g.* $\beta = 1$, $\beta = 2$, and $\beta \rightarrow \infty$ would correspond to the PDF of the Laplace, Gaussian, and Uniform distribution, respectively. The auxiliary parameters c_1 and c_2 are used to stabilize the curve fitting process and Γ is the gamma function that can be calculated as $\Gamma(z) = \int_0^\infty x^{z-1} e^{-x} dx$. Fig. 3 shows the ERF patterns for existing defocus deblurring networks, along with the fit of $f(x)$ to their central horizontal scanline and the corresponding parameter values. Please refer to the supplementary for more ERFs examples and fitted curves.

Our mission is to design a network that fully utilizes the information from the entire patch with a large receptive field, and at the same time, focuses more on the adjacent area which has a stronger influence than the peripheral area. These two properties can potentially be quantified using the estimated parameters of our fitted $f(x)$. Specifically,

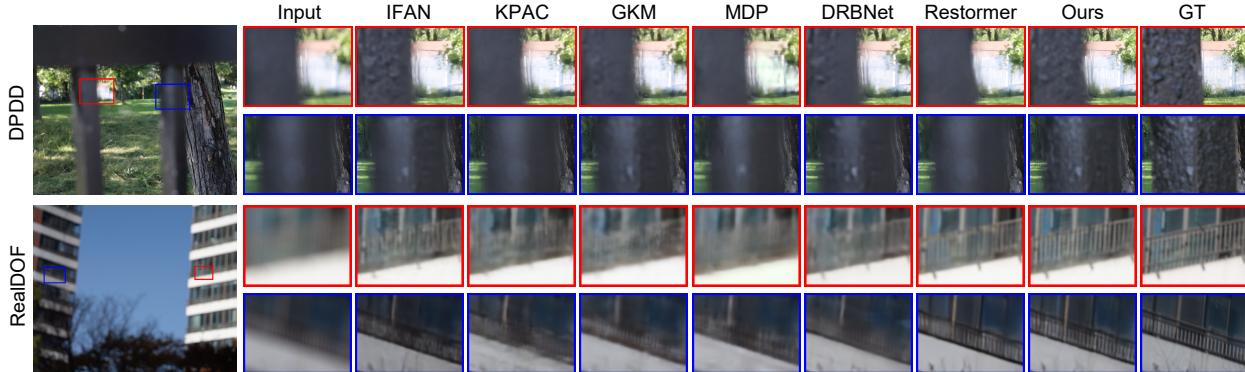


Figure 5. The visual comparison between ours and the recent defocus deblurring methods: IFAN [32], KPAC [63], GKM [48], Restormer [84], MDP [1], DRBNet [53]. Note that DRBNet in this case is trained using only the DPDD dataset. All the methods are evaluated using the code provided by their respective authors. The image samples are taken from the DPDD [2] and RealDOF [32] datasets, respectively.

the scaling factor σ is used to evaluate the breadth of ERF, where larger σ indicates better global attention ability of the network. Moreover, we opt the shape parameter β to evaluate the concentration of ERF in which smaller β produces sharper distribution in the center and indicates better concentration ability of the network. In summary, we formulate our ERF evaluation method called ERFMeter as follows:

$$\text{ERFM} = \frac{\sigma}{\sqrt{2}\beta} \log(\max(x) + 1), \quad (5)$$

Note we also consider the impact of maximum magnitude of the raw ERF response using the scale factor $\log(\max(x) + 1)$. We tested our ERFMeter on several existing defocus deblurring networks and different variants of our own network that were trained and tested on DPDD dataset. As shown in Fig. 4, the Pearson Correlation coefficient $r = 0.80$ indicates the strong correlation between the ERFM score and network performance (PSNR). While the Eq. 5 is just an empirical formula to correlate the network performance with ERF in the image deblurring tasks, we believe that our suggested metric can provide some insights into network structure design and also inspire the research community to investigate similar ERF measures that are suitable for other image-processing tasks. Besides, we only consider a 1D signal (horizontal scanline that crosses the ERF center) for demonstration purposes, the 2D version could be easily deduced.

4. Experimental Results

We evaluate our proposed method on the defocus deblurring with single or dual-view images as the input [2], as well as single-image motion deblurring task. To evaluate our method in the defocus deblurring task, we train our network on the DPDD dataset, and evaluate it on its own test set and the RealDOF dataset. For motion deblurring, we train our network on the GoPro dataset [43], and evaluate it

on its own test set, as well as the HIDE [59], RealBlur-J and RealBlur-R [51] datasets. We additionally train two other models on RealBlur-J and RealBlur-R, respectively. Some recent works, *e.g.* Restormer-TLC, MPRNet-TLC [13] and NAFNet-TLC [9], have been further refined by the test-time improvement tool dubbed TLC [13] aiming to narrow the performance gap between the cropped patches and full-resolution images during training and inference. Here we present all the methods without any test time improvement for a fairer comparison. Note that we use the code and trained weights as provided by the respective authors.

Implementation Details We adopt AdamW optimizer [40] with momentum $\beta_1 = 0.9$, $\beta_2 = 0.999$, weight decay $1e-4$, learning rate starting from $3e-4$ and gradually approach to $1e-6$ (cosine annealing [39]). We follow a similar training strategy as proposed in [84] where the patch size progressively increases [192, 256, 288, 368, 448] and the batch size decreases [5, 4, 3, 2, 1] at iterations [60k, 120k, 180k, 240k, 300k] and [180k, 360k, 540k, 720k, 900k] for the defocus and motion deblurring tasks, respectively. For defocus deblurring, we use the charbonnier loss [7] and perceptual loss [25] sequentially for 310k iterations in total, and the charbonnier loss alone for 900k iterations for motion deblurring. More training details regarding specific datasets are included in the supplementary.

4.1. Comparison to the State-of-the-Art Methods

Defocus Deblurring We evaluate our method in the defocus deblurring task for the single-image (Tab. 1) and dual-pixel (Tab. 2) input. We perform the single-image evaluation on the DPDD [2] and RealDOF [32] datasets, respectively. Specifically, in the former dataset, the defocus and all-in-focus image pairs are captured with wide and narrow apertures individually, while in the latter one by one shot through a customized dual-camera setup with a beam splitter. Note that all compared methods are trained on the

DPDD dataset except the AIFNet [54] and MDP [1] methods, which use their own training set. IFANet [32] adopts extra dual views during the training. Table 1 demonstrates that our method substantially outperforms existing CNN-based methods, improving over the state-of-the-art method DRBNet [53] by 0.68dB (+2.7%) PSNR, and slightly outperforms Transformer-based methods, yielding +0.17dB improvement over Restormer [84]. Notably, our method requires much less computational effort, saving up to 32.2% parameters and 39% MACs. Figure 5 further shows that our method is more effective than other approaches qualitatively, particularly, in handling severe defocus (the iron railings) and restoring fine texture (the fence and balcony) in Fig. 5. The performance of our dual-pixel image defocus deblurring (Tab. 2) is similar to its counterpart for the single-image input (Tab. 1), where only for Restormer [84] the SSIM metric shows slightly better results than our method. Additionally, we follow the training strategy that initiates the training on the LFDof dataset [54] followed by the DPDD dataset, showing a better generalization ability than the existing state-of-the-art DRBNet [53], as illustrated in Tab. 3 and Fig. 6. Our method offers a strong restoration ability with sharper details and clearer text.

Table 1. Single-image defocus deblurring task: Quantitative image quality and computational cost comparison.

Method	DPDD			RealDOF			Params. (M)	MACs (G)
	PSNR↑	SSIM↑	LPIPS↓	PSNR↑	SSIM↑	LPIPS↓		
DPDNet [2]	24.39	0.749	0.277	22.87	0.670	0.425	31.03	770
AIFNet [54]	24.21	0.742	0.309	23.09	0.680	0.413	41.55	1747
IFANet [32]	25.37	0.789	0.217	24.71	0.749	0.306	10.48	363
KPAC [63]	25.22	0.774	0.226	23.98	0.716	0.336	2.06	113
GKMNNet [48]	25.47	0.786	0.217	24.15	0.728	0.316	1.41	296
MDP [1]	25.35	0.763	0.303	23.73	0.685	0.435	46.86	1898
DRBNet [53]	25.47	0.787	0.246	24.70	0.744	0.337	11.69	693
Restormer [84]	25.98	0.811	0.178	25.08	0.769	0.289	26.13	1983
Ours	26.15	0.810	0.155	25.08	0.762	0.267	17.7	1208

Table 2. Dual-pixel-image defocus deblurring task: Quantitative image quality comparison. Suffix D denotes that the network takes dual-pixel images as the input.

Method	DPDD			Params. (M)
	PSNR↑	SSIM↑	LPIPS↓	
DPDNet $_D$ [2]	25.13	0.786	0.223	31.03
IFANet $_D$ [32]	25.99	0.804	0.207	10.48
KPAC $_D$ [63]	25.82	0.800	0.185	2.06
RDPD $_D$ [3]	25.41	0.771	0.255	1.41
DRBNet $_D$ [53]	26.33	0.811	0.154	11.69
Restormer $_D$ [84]	26.66	0.833	0.155	26.13
Ours $_D$	26.72	0.826	0.140	17.7

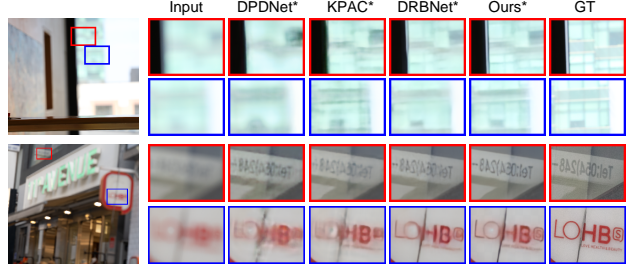


Figure 6. The visual comparison between DPDNet [2], KPAC [63], DRBNet [53] and ours when adopting the training strategy in DRBNet [53]. The former three methods are evaluated with the weights and code as provided in [53]. The sample images are from the DPDD [2] and RealDOF [32] datasets, respectively.

Table 3. The performance comparison among DPDNet [2], KPAC [63], DRBNet [53] and our method when trained on LFDof & DPDD. * denotes that each respective network is trained with the strategy as proposed in [53].

Method	DPDD			RealDOF		
	PSNR↑	SSIM↑	LPIPS↓	PSNR↑	SSIM↑	LPIPS↓
DPDNet*	24.90	0.761	0.278	24.16	0.712	0.377
KPAC*	25.47	0.780	0.220	24.64	0.735	0.319
DRBNet*	25.73	0.791	0.183	25.75	0.771	0.257
Ours*	25.89	0.792	0.154	25.83	0.769	0.245

Motion deblurring We evaluate the performance of our network for single-image motion deblurring using four benchmark datasets with synthetic blur (GoPro [43], HIDE [59]) and real-world blur (RealBlur-J and RealBlur-R [51]). We compare our network performance with the following state-of-the-art learning-based techniques: CNNs ([43], [86], [66], [59], [21], [86], [65], [21], [47], [11]), GANs ([30], [31], [88]), RNNs ([45]), and Transformers ([75], [84]). First, following [75, 84] we evaluate our method on all four datasets while training on the GoPro dataset alone. Table 4 shows that we achieve a competitive performance on the GoPro and HIDE datasets, significantly surpassing the existing CNN, GAN, and RNN solutions. For instance, we outperform the latest MSSNet [28] and NAFNet [9] (CNN) by +0.34dB / +0.27dB on the GoPro in terms of PSNR. Our method also outperforms Transformer-based Uformer / Restormer by +0.30dB / +0.43dB on the GoPro dataset, while sparing up to 66.4% / 34.6% parameters and 47.5% / 43.3% MACs. We use gray background to indicate the top two competitors and extra bold font for the champion. Second, we additionally evaluate our network on the datasets with real-world blur [51] as shown in Tab. 5. The upper part presents the outcome of training on the GoPro dataset with synthetic blur. Two Transformer-based solutions perform slightly better than ours when it comes to generalizing from synthetic to real blur. This is expected due to our compact structure, while we still obtain comparable or even better results than the remaining

competitors, for example, requiring 89.7% and 47.9% fewer MACs compared to MPRNet and MSSNet. The lower part of Tab. 5 refers to respective training on the RealBlur-J and RealBlur-R datasets in which case our network performs the best with +0.60dB / +0.15dB and +0.57dB / +0.23dB gain over MPRNet / MSSNet. Figure 7 demonstrates how our method can restore challenging examples with a plausible visual quality when compared to others (*e.g.* text and face).

Table 4. Motion deblurring comparison on the GoPro dataset. Please note the reported NAFNet is without TLC for fair network structure benchmark comparison. Please refer to its TLC version in [9].

Method	GoPro		HIDE		Params. (M)	MACs (G)
	PSNR↑	SSIM↑	PSNR↑	SSIM↑		
DeblurGAN [30]	28.70	0.858	24.51	0.871	6.06	809
DeepDeblur [43]	29.08	0.914	25.73	0.874	11.72	4729
Zhang <i>et al.</i> [87]	29.19	0.931	N/A	N/A	37.1	N/A
DeblurGAN-v2 [31]	29.55	0.934	26.61	0.875	5.08	411
SRN [66]	30.26	0.934	28.36	0.915	8.06	20134
Shen <i>et al.</i> [59]	30.26	0.940	28.89	0.930	N/A	N/A
Gao <i>et al.</i> [21]	30.90	0.935	29.11	0.913	2.84	3255
DBGAN [88]	31.10	0.942	28.94	0.915	11.59	10685
MTRNN [45]	31.15	0.945	29.15	0.918	2.6	2315
DMPHN [86]	31.20	0.940	29.09	0.924	7.23	1100
Suin <i>et al.</i> [65]	31.85	0.948	29.98	0.930	N/A	N/A
SPAIR [47]	32.06	0.953	30.29	0.931	N/A	N/A
MIMO-UNet+ [11]	32.45	0.957	29.99	0.930	16.1	2171
MPRNet [85]	32.66	0.959	30.96	0.939	20.1	10927
Uformer [75]	33.05	0.962	30.89	0.940	50.88	2143
Restormer [84]	32.92	0.961	31.22	0.942	26.13	1983
MSSNet [28]	33.01	0.961	30.79	0.938	15.59	2159
NAFNet [9]	33.08	0.963	31.22	0.943	67.89	890
Ours	33.35	0.964	31.21	0.943	17.1	1125

4.2. Ablation study

We conduct our ablation study on the DPDD dataset for defocus deblurring and the GoPro dataset for motion deblurring. We start by explaining the effectiveness of our proposed LaKD block compared to the existing UNet baseline (pure convolution and residual blocks) and then compare it to an equivalent block with dilated convolution. We further discuss the key design decisions concerning the shortcuts, kernel size, and block number. The relevant network structure could be found in the supplementary.

Effectiveness of LaKD block We adopt two UNet-like CNNs composed of pure convolution layers [52] and Res-block [35], denoted as UNet-conv and UNet-res. Table 6 demonstrates that our proposed block largely outperforms these two baselines by 3.2% (+0.82dB) and 1.3% (+0.33dB). This demonstrates the superiority of our customized CNN block.

Large kernel vs. Dilated convolution We replace our large kernel depth-wise convolution with dilated (atrous) convolutions [80], which could also expand the receptive field [56] or capture long-range information [76] through

Table 5. Motion deblurring comparison on the RealBlur-R and RealBlur-J datasets. The upper part refers to training restricted to the GoPro dataset with synthesized blur, while in the lower part training is performed using the individual datasets with real-world blur. Please note the reported NAFNet is without TLC for fair network structure benchmark comparison. Please refer to its TLC version in [9].

Method	RealBlur-R		RealBlur-J		Params. (M)	MACs (G)
	PSNR↑	SSIM↑	PSNR↑	SSIM↑		
Hu <i>et al.</i> [24]	33.67	0.916	26.41	0.803	N/A	N/A
DeepDeblur [43]	32.51	0.841	27.87	0.827	11.72	4279
DeblurGAN [30]	33.79	0.903	27.97	0.834	6.06	809
Pan <i>et al.</i> [44]	34.01	0.916	27.22	0.790	N/A	N/A
DeblurGAN-v2 [31]	35.26	0.944	28.70	0.866	5.08	411
Zhang <i>et al.</i> [87]	35.48	0.947	27.80	0.866	37.1	N/A
SRN [66]	35.66	0.947	28.56	0.867	8.06	20134
DMPHN [86]	35.70	0.948	28.42	0.860	7.23	1100
MPRNet [85]	35.99	0.952	28.70	0.873	20.1	10927
MSSNet [28]	35.93	0.953	28.79	0.879	15.6	2159
Uformer [75]	36.22	0.957	29.06	0.884	50.88	2143
Restormer [84]	36.19	0.957	28.96	0.879	26.13	1983
NAFNet [9]	36.14	0.955	28.43	0.860	67.89	890
Ours	35.91	0.954	28.78	0.878	17.1	1125
DeblurGAN-v2 [31]	36.44	0.935	29.69	0.870	5.08	411
SRN [66]	38.65	0.965	31.38	0.909	8.06	20134
MPRNet [85]	39.31	0.972	31.76	0.922	20.1	10927
MIMO-UNet++ [11]	N/A	N/A	32.05	0.921	16.1	8683
MSSNet [28]	39.76	0.972	32.10	0.928	15.6	2159
Ours	39.91	0.974	32.33	0.929	17.1	1125

Table 6. Quantitative performance of three UNet-like structures.

Method	DPDD		
	PSNR↑	SSIM↑	LPIPS↓
UNet-conv [52]	25.33	0.775	0.216
UNet-res [35]	25.82	0.797	0.178
Ours	26.15	0.810	0.155

defining spacing between the convolutional filters with various dilation rates. We adopt the hybrid dilated convolution (HDC) to avoid gridding artifacts inherited from a serialized convolution with a fixed dilation rate [73]. Here we specify the dilation rates of 1, 2, 3 in the three cascaded convolution layers accordingly inside the block and preserve the equivalent inner and middle shortcuts. Table 7 shows that our LaKD block equipped with large depth-wise convolution significantly outperforms dilated convolution in both defocus and motion deblurring tasks. This can be explained by the nature of dilated convolution, where the local or neighboring information is lost due to the sparsity in their convolution kernels.

Importance of mixing The shortcut in our LaKD module offers considerable improvement to network performance. As shown in Tab. 8, we ablate three variants of the shortcuts: (1) removing the inner shortcut inside the feature mixing module (labeled in red in Fig. 2); (2) removing the middle shortcut starting from the beginning of the LaKD block till

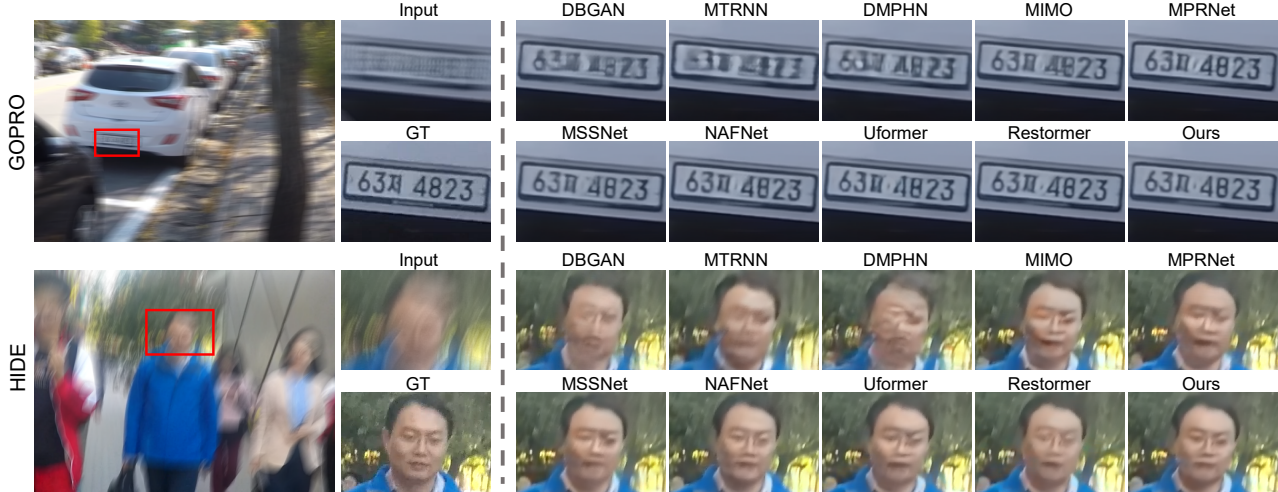


Figure 7. The visual comparison between our method and the recent motion deblurring techniques including DBGAN [88], MTRNN [45], DMPHN [86], MIMO [11], MPRNet [85], MSSNet [28], NAFNet [9], Uformer [75], and Restormer [84]. All the methods are evaluated using the code provided by their respective authors without any test-time refinement (e.g. TLC [13]) for fairer comparisons. The upper and bottom row images are taken from the GOPRO [43] and HIDE [59] datasets, respectively.

Table 7. Quantitative performance comparison between the model with dilated convolution and our LaKDNet.

Method	Defocus			Params. (M)	Motion		Params. (M)
	PSNR \uparrow	SSIM \uparrow	LPIPS \downarrow		PSNR \uparrow	SSIM \uparrow	
Dilated	25.67	0.785	0.195	21.9	32.82	0.960	21.9
Ours	26.15	0.810	0.155	17.7	33.35	0.962	17.1

the end of feature mixing module (labeled in blue in Fig. 2); (3) removing the inner and middle shortcuts. Note that we always keep the initial shortcut from the beginning to the end of the LaKD block (labeled in black in Fig. 2) as it is helpful for the final performance as demonstrated in UNet-res (Tab. 6). Table 8 shows that the performance will drop significantly without inner and middle shortcuts, even slightly worse than the baseline UNet-res (Tab. 6). This is expected since we use unusually large kernels for training, where shortcuts could potentially benefit the gradient flow and feature propagation.

Table 8. The effectiveness of shortcuts inside the LaKD block.

Method	DPDD		
	PSNR \uparrow	SSIM \uparrow	LPIPS \downarrow
w/o inner	26.01	0.807	0.156
w/o middle	26.09	0.810	0.159
w/o inner & middle	25.78	0.795	0.175
Ours	26.15	0.810	0.155

Small or large kernel size? Table 9 shows the influence

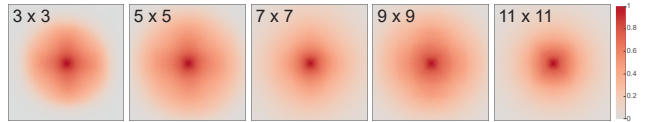


Figure 8. ERF patterns (DPDD dataset) when using different kernel sizes in our network.

of various kernel sizes on the performance. Similar as [38], we find the performance saturated on kernel size of 9×9 for defocus and 7×7 for motion deblurring. Tricks like structural reparameterization [18], kernel decomposition or dynamic sparsity [36] could possibly be applied to further enlarge the ERF without performance dropping in the future. Besides, it is worth noting that our LaKD is able to achieve a relatively larger ERF, despite using a common small kernel size of 3×3 , as shown in Fig. 3 and Fig. 12. When applying the kernel size larger than 5×5 , the receptive field is covering the whole 512×512 patch.

Table 9. Quantitative performance with respect to kernel size.

Method	Defocus			Params. (M)	Motion		Params. (M)
	PSNR \uparrow	SSIM \uparrow	LPIPS \downarrow		PSNR \uparrow	SSIM \uparrow	
3×3	25.99	0.809	0.162	16.4	33.21	0.964	16.4
5×5	26.00	0.809	0.163	16.7	33.26	0.964	16.7
7×7	26.02	0.805	0.155	17.1	33.35	0.964	17.1
9×9	26.15	0.810	0.155	17.7	33.30	0.964	17.7
11×11	26.11	0.806	0.154	18.5	N/A	N/A	N/A

Effect of block number Table 10 shows that the performance increases with the network scale, where the first column indicates the block number [$N1, N2, N3, N4$] in the

4-level symmetric encoder-decoder. A larger scale network generally results in better performance but comes at an extra cost. For defocus deblurring, [10, 14, 14, 18] achieves 0.2% (+0.05 dB) PSNR improvement with 12.9% (+2.2 M) parameter increase than [8, 12, 12, 16], while for motion deblurring, we get 0.14dB PSNR drop. We, therefore, choose [8, 12, 12, 16] as our final setting considering the trade-off on scale and performance.

Table 10. Quantitative performance with respect to block numbers.

Method	Defocus			Params. (M)	Motion		Params. (M)
	PSNR \uparrow	SSIM \uparrow	LPIPS \downarrow		PSNR \uparrow	SSIM \uparrow	
[4, 6, 6, 8]	25.84	0.795	0.166	9.7	32.86	0.961	9.4
[6, 8, 8, 10]	25.90	0.788	0.162	12	33.09	0.962	11.6
[8, 12, 12, 16]	26.15	0.810	0.155	17.7	33.35	0.964	17.1
[10, 14, 14, 18]	26.20	0.812	0.151	20	33.21	0.964	19.3

5. Conclusion

We present a lightweight CNN architecture that we contrast to computationally demanding Transformers that are recently a dominating approach in high-end motion and defocus image deblurring. Our core component LaKD block equipped with large kernels leads to a large ERF, resulting in state-of-the-art performance while maintaining simplicity and efficiency. Extensive experiments and ablation studies demonstrate the effectiveness of our method. We additionally propose ERFMeter to quantitatively characterize ERF, which is highly correlated to the network performance. However, ERFMeter is an empirical metric of network performance that strongly relies on the ERF paradigm, while ignoring the multitude of other factors. Still, we hope it can inspire the community to explore more holistic metrics that could guide efforts toward network performance improvement. In this paper, we only test our network in the image deblurring tasks, while other low-level vision applications like dehazing, deraining, or denoising, *etc.* could be considered, which we leave as future work.

Limitations Our network has a slightly weaker generalization ability than Transformer-based structures as shown in Tab. 5, despite being partially explained by the compact structure, we still have room for enhancing the generalization ability. Besides, we limit our work to evaluating network performance from the ERF point of view. Future works may further explore other aspects like network representation structure [49], loss landscape [46], *etc.*

References

[1] Abdullah Abuolaim, Mahmoud Afifi, and Michael S Brown. Improving single-image defocus deblurring: How dual-pixel images help through multi-task learning. In *Proc. Winter*

Conf. Applicat. Comput. Vis., pages 1231–1239, 2022. 5, 6, 14, 16

[2] Abdullah Abuolaim and Michael S Brown. Defocus deblurring using dual-pixel data. In *Eur. Conf. Comput. Vis.*, pages 111–126. Springer, 2020. 1, 2, 5, 6, 13, 14, 16

[3] Abdullah Abuolaim, Mauricio Delbracio, Damien Kelly, Michael S Brown, and Peyman Milanfar. Learning to reduce defocus blur by realistically modeling dual-pixel data. In *Int. Conf. Comput. Vis.*, pages 2289–2298, 2021. 6

[4] Dzmitry Bahdanau, Kyunghyun Cho, and Yoshua Bengio. Neural machine translation by jointly learning to align and translate. *arXiv preprint arXiv:1409.0473*, 2014. 2

[5] Tom Brown, Benjamin Mann, Nick Ryder, Melanie Subbiah, Jared D Kaplan, Prafulla Dhariwal, Arvind Neelakantan, Pranav Shyam, Girish Sastry, Amanda Askell, et al. Language models are few-shot learners. *Adv. Neural Inform. Process. Syst.*, 33:1877–1901, 2020. 2

[6] Nicolas Carion, Francisco Massa, Gabriel Synnaeve, Nicolas Usunier, Alexander Kirillov, and Sergey Zagoruyko. End-to-end object detection with transformers. In *Eur. Conf. Comput. Vis.*, pages 213–229. Springer, 2020. 2

[7] Pierre Charbonnier, Laure Blanc-Feraud, Gilles Aubert, and Michel Barlaud. Two deterministic half-quadratic regularization algorithms for computed imaging. In *Int. Conf. Image Process.*, volume 2, pages 168–172. IEEE, 1994. 5

[8] Hanting Chen, Yunhe Wang, Tianyu Guo, Chang Xu, Yiping Deng, Zhenhua Liu, Siwei Ma, Chunjing Xu, Chao Xu, and Wen Gao. Pre-trained image processing transformer. In *Proc. IEEE Conf. Comput. Vis. Pattern Recog.*, pages 12299–12310, 2021. 2

[9] Liangyu Chen, Xiaojie Chu, Xiangyu Zhang, and Jian Sun. Simple baselines for image restoration. *arXiv preprint arXiv:2204.04676*, 2022. 5, 6, 7, 8

[10] Sunghyun Cho and Seungyong Lee. Fast motion deblurring. *ACM Trans. Graph.*, 28(5):1–8, 2009. 2

[11] Sung-Jin Cho, Seo-Won Ji, Jun-Pyo Hong, Seung-Won Jung, and Sung-Jea Ko. Rethinking coarse-to-fine approach in single image deblurring. In *Int. Conf. Comput. Vis.*, pages 4641–4650, 2021. 1, 2, 6, 7, 8, 14, 19

[12] François Chollet. Xception: Deep learning with depthwise separable convolutions. In *Proc. IEEE Conf. Comput. Vis. Pattern Recog.*, pages 1251–1258, 2017. 2

[13] X Chu, L Chen, C Chen, and X Lu. Improving image restoration by revisiting global information aggregation. *arXiv preprint arXiv:2112.04491*, 5, 2021. 5, 8

[14] Xiangxiang Chu, Zhi Tian, Yuqing Wang, Bo Zhang, Haibing Ren, Xiaolin Wei, Huaxia Xia, and Chunhua Shen. Twins: Revisiting the design of spatial attention in vision transformers. *Adv. Neural Inform. Process. Syst.*, 34:9355–9366, 2021. 2

[15] Yann N Dauphin, Angela Fan, Michael Auli, and David Grangier. Language modeling with gated convolutional networks. In *Int. Conf. Mach. Learn.*, pages 933–941. PMLR, 2017. 3, 4

[16] Jacob Devlin, Ming-Wei Chang, Kenton Lee, and Kristina Toutanova. Bert: Pre-training of deep bidirectional transformers for language understanding. *arXiv preprint arXiv:1810.04805*, 2018. 2

- [17] Xiaohan Ding, Xiangyu Zhang, Jungong Han, and Guiguang Ding. Scaling up your kernels to 31x31: Revisiting large kernel design in cnns. In *Proc. IEEE Conf. Comput. Vis. Pattern Recog.*, pages 11963–11975, 2022. 2, 3, 4
- [18] Xiaohan Ding, Xiangyu Zhang, Ningning Ma, Jungong Han, Guiguang Ding, and Jian Sun. Repvgg: Making vgg-style convnets great again. In *Proc. IEEE Conf. Comput. Vis. Pattern Recog.*, pages 13733–13742, 2021. 4, 8
- [19] Alexey Dosovitskiy, Lucas Beyer, Alexander Kolesnikov, Dirk Weissenborn, Xiaohua Zhai, Thomas Unterthiner, Mostafa Dehghani, Matthias Minderer, Georg Heigold, Sylvain Gelly, et al. An image is worth 16x16 words: Transformers for image recognition at scale. In *Int. Conf. Learn. Represent.*, 2021. 2
- [20] Uwe Franke and Armin Joos. Real-time stereo vision for urban traffic scene understanding. In *IEEE Intell. Vehicles Symposium*, pages 273–278. IEEE, 2000. 1
- [21] Hongyun Gao, Xin Tao, Xiaoyong Shen, and Jiaya Jia. Dynamic scene deblurring with parameter selective sharing and nested skip connections. In *Proc. IEEE Conf. Comput. Vis. Pattern Recog.*, pages 3848–3856, 2019. 6, 7, 14, 19
- [22] Kaiming He, Xiangyu Zhang, Shaoqing Ren, and Jian Sun. Deep residual learning for image recognition. In *Proc. IEEE Conf. Comput. Vis. Pattern Recog.*, pages 770–778, 2016. 2
- [23] Dan Hendrycks and Kevin Gimpel. Gaussian error linear units (gelus). *arXiv preprint arXiv:1606.08415*, 2016. 4
- [24] Zhe Hu, Sunghyun Cho, Jue Wang, and Ming-Hsuan Yang. Deblurring low-light images with light streaks. In *Proc. IEEE Conf. Comput. Vis. Pattern Recog.*, pages 3382–3389, 2014. 7
- [25] Justin Johnson, Alexandre Alahi, and Li Fei-Fei. Perceptual losses for real-time style transfer and super-resolution. In *Eur. Conf. Comput. Vis.*, pages 694–711. Springer, 2016. 5
- [26] Ali Karaali and Claudio Rosito Jung. Edge-based defocus blur estimation with adaptive scale selection. *IEEE Trans. Image Process.*, 27(3):1126–1137, 2017. 2
- [27] Salman Khan, Muzammal Naseer, Munawar Hayat, Syed Waqas Zamir, Fahad Shahbaz Khan, and Mubarak Shah. Transformers in vision: A survey. *ACM Comput. Surv.*, 54(10s), sep 2022. 2
- [28] Kiyeon Kim, Seungyong Lee, and Sunghyun Cho. Mssnet: Multi-scale-stage network for single image deblurring. *arXiv preprint arXiv:2202.09652*, 2022. 1, 2, 6, 7, 8, 23, 24
- [29] Alex Krizhevsky, Ilya Sutskever, and Geoffrey E Hinton. Imagenet classification with deep convolutional neural networks. *Communications of the ACM*, 60(6):84–90, 2017. 3
- [30] Orest Kupyn, Volodymyr Budzan, Mykola Mykhailych, Dmytro Mishkin, and Jiří Matas. Deblurgan: Blind motion deblurring using conditional adversarial networks. In *Proc. IEEE Conf. Comput. Vis. Pattern Recog.*, pages 8183–8192, 2018. 6, 7, 14, 19
- [31] Orest Kupyn, Tetiana Martyniuk, Junru Wu, and Zhangyang Wang. Deblurgan-v2: Deblurring (orders-of-magnitude) faster and better. In *Int. Conf. Comput. Vis.*, pages 8878–8887, 2019. 6, 7
- [32] Junyong Lee, Hyeongseok Son, Jaesung Rim, Sunghyun Cho, and Seungyong Lee. Iterative filter adaptive network for single image defocus deblurring. In *Proc. IEEE Conf. Comput. Vis. Pattern Recog.*, pages 2034–2042, 2021. 1, 2, 5, 6, 13, 14, 16
- [33] ChuMiao Li. A survey on image deblurring. *arXiv preprint arXiv:2202.07456*, 2022. 1
- [34] Jingyun Liang, Jiezhong Cao, Guolei Sun, Kai Zhang, Luc Van Gool, and Radu Timofte. Swinir: Image restoration using swin transformer. In *Int. Conf. Comput. Vis.*, pages 1833–1844, 2021. 2, 3
- [35] Bee Lim, Sanghyun Son, Heewon Kim, Seungjun Nah, and Kyoung Mu Lee. Enhanced deep residual networks for single image super-resolution. In *IEEE Conf. Comput. Vis. Pattern Recog. Worksh.*, pages 136–144, 2017. 7
- [36] Shiwei Liu, Tianlong Chen, Xiaohan Chen, Xuxi Chen, Qiao Xiao, Boqian Wu, Mykola Pechenizkiy, Decebal Mocanu, and Zhangyang Wang. More convnets in the 2020s: Scaling up kernels beyond 51x51 using sparsity. *arXiv preprint arXiv:2207.03620*, 2022. 2, 3, 4, 8
- [37] Ze Liu, Yutong Lin, Yue Cao, Han Hu, Yixuan Wei, Zheng Zhang, Stephen Lin, and Baining Guo. Swin transformer: Hierarchical vision transformer using shifted windows. In *Int. Conf. Comput. Vis.*, pages 10012–10022, 2021. 2, 3
- [38] Zhuang Liu, Hanzi Mao, Chao-Yuan Wu, Christoph Feichtenhofer, Trevor Darrell, and Saining Xie. A convnet for the 2020s. In *Proc. IEEE Conf. Comput. Vis. Pattern Recog.*, pages 11976–11986, 2022. 2, 3, 8
- [39] Ilya Loshchilov and Frank Hutter. Sgdr: Stochastic gradient descent with warm restarts. *arXiv preprint arXiv:1608.03983*, 2016. 5
- [40] Ilya Loshchilov and Frank Hutter. Decoupled weight decay regularization. *arXiv preprint arXiv:1711.05101*, 2017. 5
- [41] Wenjie Luo, Yujia Li, Raquel Urtasun, and Richard Zemel. Understanding the effective receptive field in deep convolutional neural networks. *Adv. Neural Inform. Process. Syst.*, 29, 2016. 14
- [42] Pengyuan Lyu, Minghui Liao, Cong Yao, Wenhao Wu, and Xiang Bai. Mask textspotter: An end-to-end trainable neural network for spotting text with arbitrary shapes. In *Proceedings of the Eur. Conf. Comput. Vis. (ECCV)*, pages 67–83, 2018. 1
- [43] Seungjun Nah, Tae Hyun Kim, and Kyoung Mu Lee. Deep multi-scale convolutional neural network for dynamic scene deblurring. In *Proc. IEEE Conf. Comput. Vis. Pattern Recog.*, pages 3883–3891, 2017. 1, 2, 5, 6, 7, 8, 13, 14
- [44] Jinshan Pan, Deqing Sun, Hanspeter Pfister, and Ming-Hsuan Yang. Blind image deblurring using dark channel prior. In *Proc. IEEE Conf. Comput. Vis. Pattern Recog.*, pages 1628–1636, 2016. 7
- [45] Dongwon Park, Dong Un Kang, Jisoo Kim, and Se Young Chun. Multi-temporal recurrent neural networks for progressive non-uniform single image deblurring with incremental temporal training. In *Eur. Conf. Comput. Vis.*, pages 327–343. Springer, 2020. 6, 7, 8, 14
- [46] Namuk Park and Songkuk Kim. How do vision transformers work? *arXiv preprint arXiv:2202.06709*, 2022. 9
- [47] Kuldeep Purohit, Maitreya Suin, AN Rajagopalan, and Vishnu Naresh Boddeti. Spatially-adaptive image restora-

- tion using distortion-guided networks. In *Int. Conf. Comput. Vis.*, pages 2309–2319, 2021. 6, 7
- [48] Yuhui Quan, Zicong Wu, and Hui Ji. Gaussian kernel mixture network for single image defocus deblurring. In *Proc. Int. Conf. Neural Inf. Process. Syst.*, volume 34, pages 20812–20824, 2021. 2, 5, 6
- [49] Maithra Raghu, Thomas Unterthiner, Simon Kornblith, Chiyuan Zhang, and Alexey Dosovitskiy. Do vision transformers see like convolutional neural networks? *Adv. Neural Inform. Process. Syst.*, 34:12116–12128, 2021. 2, 9
- [50] Joseph Redmon, Santosh Divvala, Ross Girshick, and Ali Farhadi. You only look once: Unified, real-time object detection. In *Proc. IEEE Conf. Comput. Vis. Pattern Recog.*, June 2016. 1
- [51] Jaesung Rim, Haeyun Lee, Jucheol Won, and Sunghyun Cho. Real-world blur dataset for learning and benchmarking deblurring algorithms. In *Eur. Conf. Comput. Vis.*, pages 184–201. Springer, 2020. 5, 6, 13, 14
- [52] Olaf Ronneberger, Philipp Fischer, and Thomas Brox. U-net: Convolutional networks for biomedical image segmentation. In *Int. Conf. Medical imag. comput. computer-assisted intervention*, pages 234–241. Springer, 2015. 3, 7
- [53] Lingyan Ruan, Bin Chen, Jizhou Li, and Miuling Lam. Learning to deblur using light field generated and real defocus images. In *Proc. IEEE Conf. Comput. Vis. Pattern Recog.*, pages 16304–16313, 2022. 1, 2, 5, 6, 13, 14, 15, 16, 27, 28, 29, 30
- [54] Lingyan Ruan, Bin Chen, Jizhou Li, and Miu-Ling Lam. Aifnet: All-in-focus image restoration network using a light field-based dataset. *IEEE Trans. Comput. Imag.*, 7:675–688, 2021. 6, 13, 14
- [55] Mark Sandler, Andrew Howard, Menglong Zhu, Andrey Zhmoginov, and Liang-Chieh Chen. Mobilenetv2: Inverted residuals and linear bottlenecks. In *Proc. IEEE Conf. Comput. Vis. Pattern Recog.*, pages 4510–4520, 2018. 1, 2
- [56] George Seif and Dimitrios Androutsos. Large receptive field networks for high-scale image super-resolution. In *IEEE Conf. Comput. Vis. Pattern Recog. Worksh.*, pages 763–772, 2018. 7
- [57] Pierre Sermanet, David Eigen, Xiang Zhang, Michaël Mathieu, Rob Fergus, and Yann LeCun. Overfeat: Integrated recognition, localization and detection using convolutional networks. *arXiv preprint arXiv:1312.6229*, 2013. 1
- [58] Qi Shan, Jiaya Jia, and Aseem Agarwala. High-quality motion deblurring from a single image. *ACM Trans. Graph.*, 27(3):1–10, 2008. 2
- [59] Ziyi Shen, Wenguan Wang, Xiankai Lu, Jianbing Shen, Haibin Ling, Tingfa Xu, and Ling Shao. Human-aware motion deblurring. In *Int. Conf. Comput. Vis.*, pages 5572–5581, 2019. 5, 6, 7, 8, 13, 14
- [60] Jianping Shi, Li Xu, and Jiaya Jia. Discriminative blur detection features. In *Proc. IEEE Conf. Comput. Vis. Pattern Recog.*, pages 2965–2972, 2014. 13, 14
- [61] Wenzhe Shi, Jose Caballero, Ferenc Huszár, Johannes Totz, Andrew P Aitken, Rob Bishop, Daniel Rueckert, and Zehan Wang. Real-time single image and video super-resolution using an efficient sub-pixel convolutional neural network. In *Proc. IEEE Conf. Comput. Vis. Pattern Recog.*, pages 1874–1883, 2016. 3
- [62] Karen Simonyan and Andrew Zisserman. Very deep convolutional networks for large-scale image recognition. *arXiv preprint arXiv:1409.1556*, 2014. 3
- [63] Hyeongseok Son, Junyong Lee, Sunghyun Cho, and Seungyong Lee. Single image defocus deblurring using kernel-sharing parallel atrous convolutions. In *Int. Conf. Comput. Vis.*, pages 2642–2650, 2021. 1, 2, 5, 6, 14, 16
- [64] Robin Strudel, Ricardo Garcia, Ivan Laptev, and Cordelia Schmid. Segmenter: Transformer for semantic segmentation. In *Int. Conf. Comput. Vis.*, pages 7262–7272, 2021. 3
- [65] Maitreya Suin, Kuldeep Purohit, and AN Rajagopalan. Spatially-attentive patch-hierarchical network for adaptive motion deblurring. In *Proc. IEEE Conf. Comput. Vis. Pattern Recog.*, pages 3606–3615, 2020. 6, 7
- [66] Xin Tao, Hongyi Gao, Xiaoyong Shen, Jue Wang, and Jiaya Jia. Scale-recurrent network for deep image deblurring. In *PProc. IEEE Conf. Comput. Vis. Pattern Recog.*, pages 8174–8182, 2018. 6, 7
- [67] Christopher Thorpe, Feng Li, Zijia Li, Zhan Yu, David Saunders, and Jingyi Yu. A coprime blur scheme for data security in video surveillance. *IEEE Trans. Pattern Anal. Mach. Intell.*, 35(12):3066–3072, 2013. 1
- [68] Ilya O Tolstikhin, Neil Houlsby, Alexander Kolesnikov, Lucas Beyer, Xiaohua Zhai, Thomas Unterthiner, Jessica Yung, Andreas Steiner, Daniel Keysers, Jakob Uszkoreit, et al. Mlp-mixer: An all-mlp architecture for vision. *Adv. Neural Inform. Process. Syst.*, 34:24261–24272, 2021. 2, 3
- [69] Hugo Touvron, Matthieu Cord, Matthijs Douze, Francisco Massa, Alexandre Sablayrolles, and Herve Jegou. Training data-efficient image transformers distillation through attention. In *Int Conf. Mach. Learn.*, pages 10347–10357. PMLR, 2021. 2
- [70] Asher Trockman and J Zico Kolter. Patches are all you need? *arXiv preprint arXiv:2201.09792*, 2022. 2, 4
- [71] Ashish Vaswani, Prajit Ramachandran, Aravind Srinivas, Niki Parmar, Blake Hechtman, and Jonathon Shlens. Scaling local self-attention for parameter efficient visual backbones. In *Proc. IEEE Conf. Comput. Vis. Pattern Recog.*, pages 12894–12904, 2021. 2
- [72] Ashish Vaswani, Noam Shazeer, Niki Parmar, Jakob Uszkoreit, Llion Jones, Aidan N Gomez, Łukasz Kaiser, and Illia Polosukhin. Attention is all you need. *Adv. Neural Inform. Process. Syst.*, 30, 2017. 2
- [73] Panqu Wang, Pengfei Chen, Ye Yuan, Ding Liu, Zehua Huang, Xiaodi Hou, and Garrison Cottrell. Understanding convolution for semantic segmentation. In *2018 IEEE winter conference on applications of computer vision (WACV)*, pages 1451–1460, 2018. 7
- [74] Wenhai Wang, Enze Xie, Xiang Li, Deng-Ping Fan, Kaitao Song, Ding Liang, Tong Lu, Ping Luo, and Ling Shao. Pyramid vision transformer: A versatile backbone for dense prediction without convolutions. In *Int. Conf. Comput. Vis.*, pages 568–578, 2021. 3
- [75] Zhendong Wang, Xiaodong Cun, Jianmin Bao, Wengang Zhou, Jianzhuang Liu, and Houqiang Li. Uformer: A general

- u-shaped transformer for image restoration. In *Proc. IEEE Conf. Comput. Vis. Pattern Recog.*, pages 17683–17693, 2022. [2](#), [4](#), [6](#), [7](#), [8](#), [13](#)
- [76] Zifeng Wu, Chunhua Shen, and Anton van den Hengel. Bridging category-level and instance-level semantic image segmentation. *arXiv preprint arXiv:1605.06885*, 2016. [7](#)
- [77] Enze Xie, Wenhai Wang, Zhiding Yu, Anima Anandkumar, Jose M Alvarez, and Ping Luo. Segformer: Simple and efficient design for semantic segmentation with transformers. *Adv. Neural Inform. Process. Syst.*, 34:12077–12090, 2021. [2](#)
- [78] Li Xu and Jiaya Jia. Two-phase kernel estimation for robust motion deblurring. In *Eur. Conf. Comput. Vis.*, pages 157–170. Springer, 2010. [2](#)
- [79] Fuzhi Yang, Huan Yang, Jianlong Fu, Hongtao Lu, and Baining Guo. Learning texture transformer network for image super-resolution. In *Proc. IEEE Conf. Comput. Vis. Pattern Recog.*, pages 5791–5800, 2020. [2](#)
- [80] Fisher Yu and Vladlen Koltun. Multi-scale context aggregation by dilated convolutions. *arXiv preprint arXiv:1511.07122*, 2015. [7](#)
- [81] Li Yuan, Yunpeng Chen, Tao Wang, Weihao Yu, Yujun Shi, Zi-Hang Jiang, Francis EH Tay, Jiashi Feng, and Shuicheng Yan. Tokens-to-token vit: Training vision transformers from scratch on imagenet. In *Int. Conf. Comput. Vis.*, pages 558–567, 2021. [3](#)
- [82] Li Yuan, Qibin Hou, Zihang Jiang, Jiashi Feng, and Shuicheng Yan. Volo: Vision outlooker for visual recognition. *IEEE Trans. Pattern Anal. Mach. Intell.*, 2022. [2](#)
- [83] Lu Yuan, Jian Sun, Long Quan, and Heung-Yeung Shum. Image deblurring with blurred/noisy image pairs. *ACM Trans. Graph.*, 26(3):1–es, 2007. [1](#)
- [84] Syed Waqas Zamir, Aditya Arora, Salman Khan, Munawar Hayat, Fahad Shahbaz Khan, and Ming-Hsuan Yang. Restormer: Efficient transformer for high-resolution image restoration. In *Proc. IEEE Conf. Comput. Vis. Pattern Recog.*, pages 5728–5739, 2022. [2](#), [3](#), [4](#), [5](#), [6](#), [7](#), [8](#), [13](#), [14](#), [16](#), [19](#), [21](#), [22](#), [25](#), [26](#), [30](#)
- [85] Syed Waqas Zamir, Aditya Arora, Salman Khan, Munawar Hayat, Fahad Shahbaz Khan, Ming-Hsuan Yang, and Ling Shao. Multi-stage progressive image restoration. In *Proc. IEEE Conf. Comput. Vis. Pattern Recog.*, pages 14821–14831, 2021. [1](#), [2](#), [7](#), [8](#), [13](#)
- [86] Hongguang Zhang, Yuchao Dai, Hongdong Li, and Piotr Koniusz. Deep stacked hierarchical multi-patch network for image deblurring. In *Proc. IEEE Conf. Comput. Vis. Pattern Recog.*, pages 5978–5986, 2019. [1](#), [2](#), [6](#), [7](#), [8](#), [14](#)
- [87] Jiawei Zhang, Jinshan Pan, Jimmy Ren, Yibing Song, Linchao Bao, Rynson WH Lau, and Ming-Hsuan Yang. Dynamic scene deblurring using spatially variant recurrent neural networks. In *Proc. IEEE Conf. Comput. Vis. Pattern Recog.*, pages 2521–2529, 2018. [7](#)
- [88] Kaihao Zhang, Wenhan Luo, Yiran Zhong, Lin Ma, Bjorn Stenger, Wei Liu, and Hongdong Li. Deblurring by realistic blurring. In *Proc. IEEE Conf. Comput. Vis. Pattern Recog.*, pages 2737–2746, 2020. [6](#), [7](#), [8](#)
- [89] Sixiao Zheng, Jiachen Lu, Hengshuang Zhao, Xiatian Zhu, Zekun Luo, Yabiao Wang, Yanwei Fu, Jianfeng Feng, Tao Xiang, Philip HS Torr, et al. Rethinking semantic segmentation from a sequence-to-sequence perspective with transformers. In *Proc. IEEE Conf. Comput. Vis. Pattern Recog.*, pages 6881–6890, 2021. [2](#)
- [90] Xizhou Zhu, Weijie Su, Lewei Lu, Bin Li, Xiaogang Wang, and Jifeng Dai. Deformable detr: Deformable transformers for end-to-end object detection. In *Int. Conf. Learn. Represent.*, 2021. [2](#)

Revisiting Image Deblurring with an Efficient ConvNet

- Supplementary Material

In this supplementary material, we provide more details on the following topics: (1) all datasets that we employed in the network training (Sec.5.1), (2) the dilated structure that we consider in the ablation study (Sec.5.2), (3) the quantitative comparison on the LFDof dataset [54] (Sec. 5.3), (4) the effective receptive field (ERF) and its evolution during the training (Sec. 6), and (5) additional qualitative comparisons of motion deblurring evaluated on the GoPro [43], HIDE [59], and RealBlur [51] datasets, as well as defocus deblurring evaluated on the DPDD [2], RealDOF [32], and CUHK [60] datasets (Sec. 7).

We will make our code and weights publicly available.

5.1. Training

Here we provide more details on all the training and evaluation datasets for image motion and defocus deblurring tasks we use in this work.

Defocus deblurring We consider four defocus-related datasets. The most popular one is DPDD [2], which collects blurry-sharp pairs separately with different aperture sizes using a DSLR camera. It has 350 training samples, and 76 testing samples for single-image defocus deblurring, as well as the dual-pixel version for dual-pixel defocus deblurring. RealDOF captures the data pairs in a single shot with a dual-camera setup, offering 50 high-resolution test samples. CUHK is collected for blur detection and provides 706 evaluated low-resolution samples acquired from the Internet. Note that RealDOF and CUHK have only testing samples and, thereby, are good for evaluating the generalization ability. LFDof is a synthetic defocus blur dataset (11261 training samples and 725 testing samples) generated using a set of light field images, which in our experiment is adopted for the two-stage training strategy as proposed in [53].

Motion deblurring We consider three benchmark datasets – GoPro [43], HIDE [59], and RealBlur [51]. The GoPro dataset features a synthetic blur that integrates adjacent frames from high-framerate videos to produce motion blur and contains 2013 blurry-sharp training pairs and 1111

testing samples. The HIDE dataset is synthesized following a similar method as the GoPro dataset but emphasizes human-aware deblurring, including large amounts of walking pedestrians, resulting in 6397 training and 2025 testing pairs. Here we follow [75, 84, 85] and train our network on the GoPro dataset alone and directly evaluate the HIDE test set for demonstrating the generalization ability. The RealBlur dataset captures real motion blur and sharp images with a dual DSLR camera (Sony A7RM3) setup, which can be obtained simultaneously with different shutter speeds. It offers two subsets sharing the same content, one is output as JPEG images through a camera ISP, and the other is generated as raw images with white balance, demosaicing, denoising, geometric alignment, *etc.*, resulting in 3758 training samples and 980 testing samples for each set dubbed Real-J and Real-R. In our experiment, we train our network on the GoPro dataset and directly test it on the RealBlur dataset. We also train it on each RealBlur set for extra 450k iterations from the pre-trained weight using GoPro dataset as suggested in [51] and evaluate their associated testing sets.

In Tab. S11 we summarize the training and testing datasets used in the main manuscript.

5.2. Ablation of network structure

Here we ablate our network with respect to its structure and layer number.

Version with dilated convolution layers As opposed to the LaKD block described in the main paper, here, we present its alternative version with dilated convolution layers (Fig. S9). Note that both versions aim to expand the effective receptive field. The dilated version adopts the same structure except for the feature mixing module that consists of three dilated convolution layers with increasing dilation rates. The results in Tab. 7 (refer to the main manuscript) further indicate the superiority of LaKD block.

Layer number We ablate the layer number required in the feature mixing module, specifically on depthwise and point-

Table 11. Summary of training and testing datasets for motion and defocus deblurring tasks.

Datasets		Training	Testing
Motion	GoPro [43]	2103	1111
	HIDE [59]	0	2025
	RealBlur-J [51]	3758	980
	RealBlur-R [51]	3758	980
Defocus	DPDD [2]	350	76
	RealDOF [32]	0	50
	LFDOF [54]	11261	725
	CUHK [60]	0	704

Tab. / Fig.		Training	Testing
Motion	Tab. 1, Tab. 2 (upper), Fig. 6, Tab. 7, 9, 10	[43]	[43] & [59] & [51]
	Tab. 2 (lower), Fig. S17, S18	[43]	[43]
	Fig. S15, S16	[51]	[51]
		[43]	[43] [59]
Defocus	Tab. 3, 4, 6 – 10, S12, Fig. 5, S19, S20	[2]	[2] & [32]
	Tab. 5, Fig. 7, S21, S22, S23, S24	[2] & [54]	[2], [32], [60]
	Tab. S13	[54]	[54]

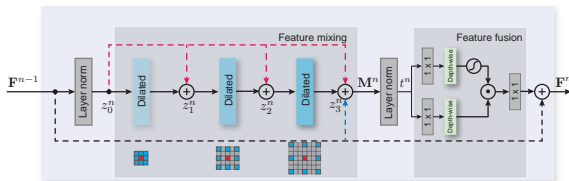


Figure 9. The structure of dilated convolution layers that can be compared with the corresponding structure in the LaKD block (refer to Fig. 2 in the main manuscript).

wise convolution. For example, the label “one” in Tab. S12 denotes that the feature mixing module has one depthwise and one pointwise convolution layer. Table S12 shows that feature mixing equipped with two sequential depthwise and pointwise layers can reach the best performance.

Table 12. Layer number ablation in the feature mixing module.

Number	DPDD			Params. (M)	MACs (G)
	PSNR \uparrow	SSIM \uparrow	LPIPS \downarrow		
one	26.10	0.808	0.155	15.4	1004
two (ours)	26.15	0.810	0.155	17.7	1208
three	26.09	0.806	0.156	20.1	1413

5.3. Performance on the LFDOF dataset

Following [53], we additionally investigate our network performance on the LFDOF dataset. AIFNet [54] has two subnets, sharing a similar spirit to the conventional methods that explicitly estimate the defocus map and then perform non-blind deconvolution. DRBNet [53] adopts an end-to-end solution and resorts to per-pixel kernel estimation to account for the spatially-varying blur. Our method is also an end-to-end solution that employs the LaKD block with a large effective receptive field, which leads to much better performance, as shown in Tab. S13.

Table 13. Quantitative comparison between AIFNet [54], DRBNet [53], and our network evaluated on 725 images from the LFDOF test set.

Method	LFDOF		
	PSNR \uparrow	SSIM \uparrow	LPIPS \downarrow
AIFNet [54]	29.69	0.880	0.151
DRBNet [53]	30.40	0.891	0.145
Ours	31.87	0.912	0.115

6. ERF fitting details

In this section, we provide more details of our ERF visualization, GND-PDF fitting, and ERFMeter. We visualize all the ERFs and GND-PDF fittings of defocus deblurring networks [1, 2, 53, 63, 84] in Fig. S10, variants of our networks that used for ablation study in Fig. S11, and our network with different kernel sizes in Fig. S12, correspondingly, all the parameters of GND-PDF fitting could be find in Tab. S14, Tab. S15, and Tab. S16. Besides, we also select several representative networks for motion deblurring [11, 21, 30, 84] and visualize their ERFs in Fig. S13. Note that the network structures are highly diverse, especially for networks on motion deblurring *e.g.* multi-patch [86], multi-scale [43], recurrent scheme [45]. In this paper, we intend to reduce the diversity and only select networks with overall U-Net architecture so that the visualized ERFs are comparable.

We investigate the ERF [41] on the feature extracted from their bottleneck layer (the layer right before the first up-sampling in the decoder), which could potentially reveal the largest ERF they can achieve. The layer names corresponding to the bottleneck layer in each method are list in Tab. S14 to Tab. S17. The ERFs of networks for defocus deblurring are averaged from 912 image patches in size 512×512 , which are augmented from 76 testing images in DPDD dataset [2] to further eliminate the dependence on input content, while ERFs of networks for motion deblurring are averaged from 1111 image patches in size 512×512 from GoPro dataset [43]. When doing GND-PDF curve fitting, the x-axis is empirically scaled from $[1, 512]$ to $[-30, 30]$ for higher fitting accuracy. We show the goodness of fitting R^2 for each network in Tab. S14 to Tab. S17. **ERF evolution during training** We additionally demonstrate the ERF evolution during training for the motion and defocus deblurring tasks, as shown in Fig. S14. The ERF expands progressively with the training iterations and becomes much larger than at the initial stages. This observation is aligned with [41].

7. Additional qualitative results

In this section we show more qualitative results on motion and defocus deblurring. Note that we mainly compare our method with Restormer [84] as it achieves state-of-art performance.

Motion deblurring We include additional visual results that are obtained using image samples from the GoPro (Fig. S15), HIDE (Fig. S16), Real-J (Fig. S17), and Real-R (Fig. S18) datasets. Those results complement Tabs. 1 and 2 in the main manuscript.

Defocus deblurring We include visual results for single-image defocus deblurring for image samples from the DPDD (Fig. S19) and RealDOF (Fig. S20) datasets. Those results complement Tab. 3. We also provide visual results for dual-pixel defocus deblurring for image samples from the DPDD (Fig. S25) dataset, which complement Tab. 4. We further compare our method with DRBNet [53] adopting the two-stage training strategy proposed in [53], and we evaluate both methods using image samples from the DPDD (Fig. S21), RealDOF (Fig. S22), and CUHK (Fig. S23, S24) datasets, which complement Tab. 5.

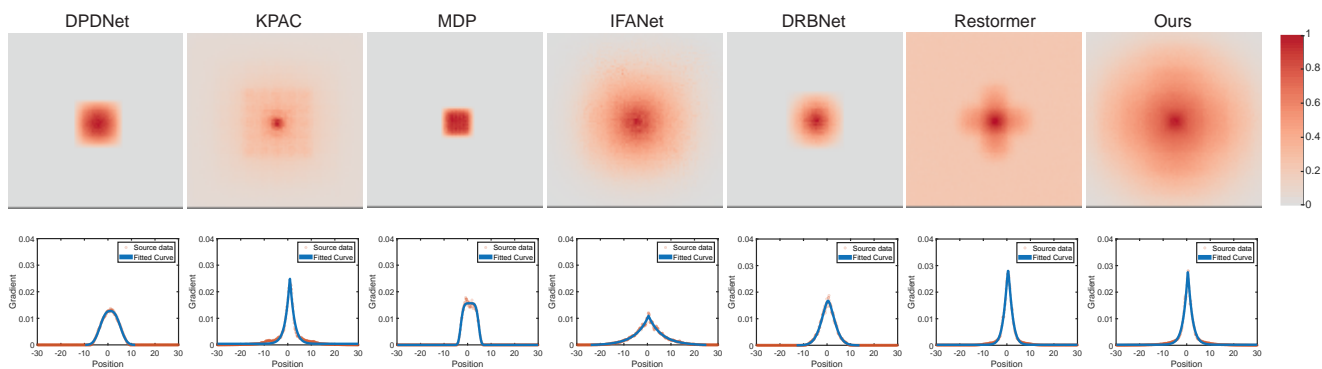
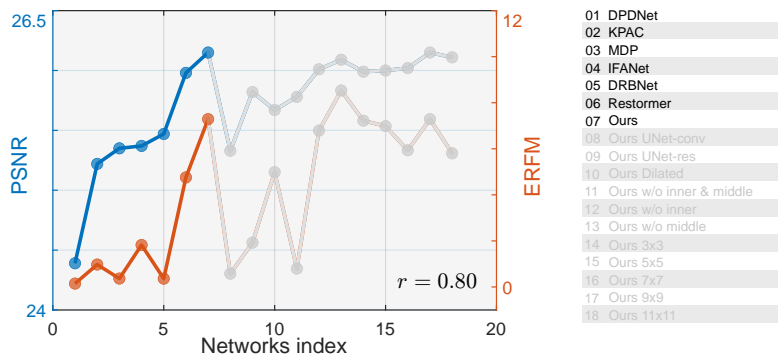


Figure 10. Demonstration of ERF patterns and the fitted GND-PDF curves: Here, different defocus deblurring networks are considered. Note that, the ERF patterns are in log scale for better visualization, while the GND-PDF curves are in linear scale.

Table 14. ERF fitting parameters and statistics for defocus deblurring networks.

Method	Layer Name	σ	β	μ	c_1	c_2 (e-5)	R^2	PSNR	ERFM
DPDNet [2]	conv5_2	5.2054	2.6054	0.9550	0.1188	-2.61	0.9978	24.39	0.1469
KPAC [63]	conv4_4	1.8945	1.0838	0.8993	0.0923	41.47	0.9774	25.22	0.9737
MDP [1]	conv15	4.0575	4.9008	0.9371	0.1174	-0.32	0.9956	25.35	0.3658
IFANet [32]	conv_res	5.6632	0.9690	0.4738	0.1291	-18.31	0.9885	25.37	1.8221
DRBNet [53]	conv4_4	3.8936	1.5960	0.4254	0.1183	-1.79	0.9942	25.47	0.3615
Restormer [84]	latent	1.9964	1.2687	0.5252	0.1057	19.14	0.9953	25.98	4.7581
Ours	bt_neck	1.9138	1.0812	0.5105	0.1044	21.27	0.9914	26.15	7.2870

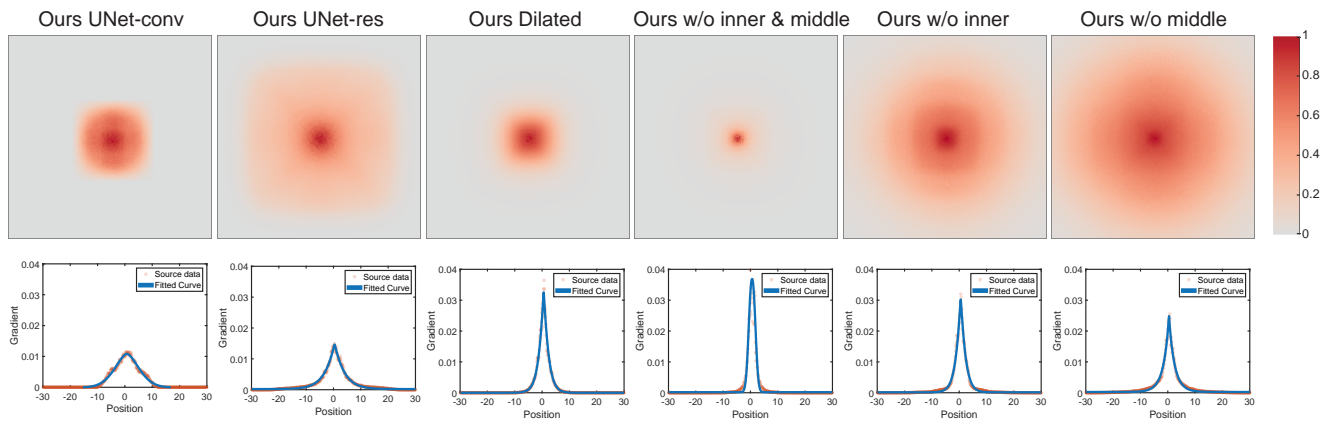
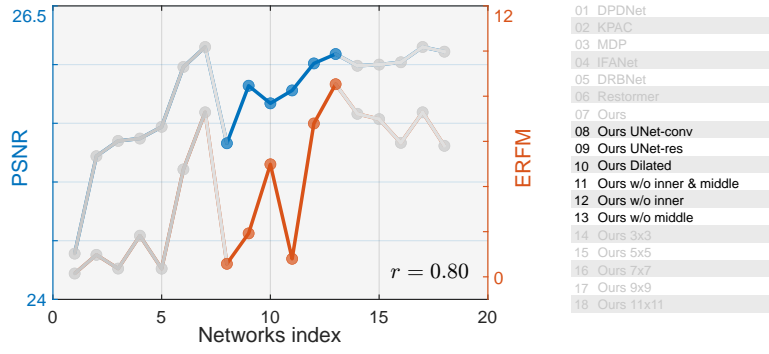


Figure 11. Demonstration of ERF patterns and the fitted GND-PDF curves: Here, different variants of our network are considered.

Table 15. ERF fitting parameters and statistics for variants of our network.

Method	Layer Name	σ	β	μ	c_1	c_2 (e-5)	R^2	PSNR	ERFM
UNet-conv	bt_neck	6.2515	1.6787	0.7357	0.1224	-8.73	0.9841	25.33	0.5774
UNet-res	bt_neck	3.6274	1.0466	0.4065	0.1048	20.60	0.9873	25.82	1.9244
Ours-dilated	bt_neck	1.8397	1.1123	0.5869	0.1170	0.30	0.9812	25.67	4.9839
Ours w/o both	bt_neck	1.6120	2.1925	0.5965	0.1067	17.43	0.9047	25.78	0.7989
Ours w/o inner	bt_neck	1.8337	1.1069	0.5574	0.1089	13.79	0.9916	26.01	6.7925
Ours w/o middle	bt_neck	1.9742	0.9474	0.4418	0.1025	24.41	0.9845	26.09	8.5311

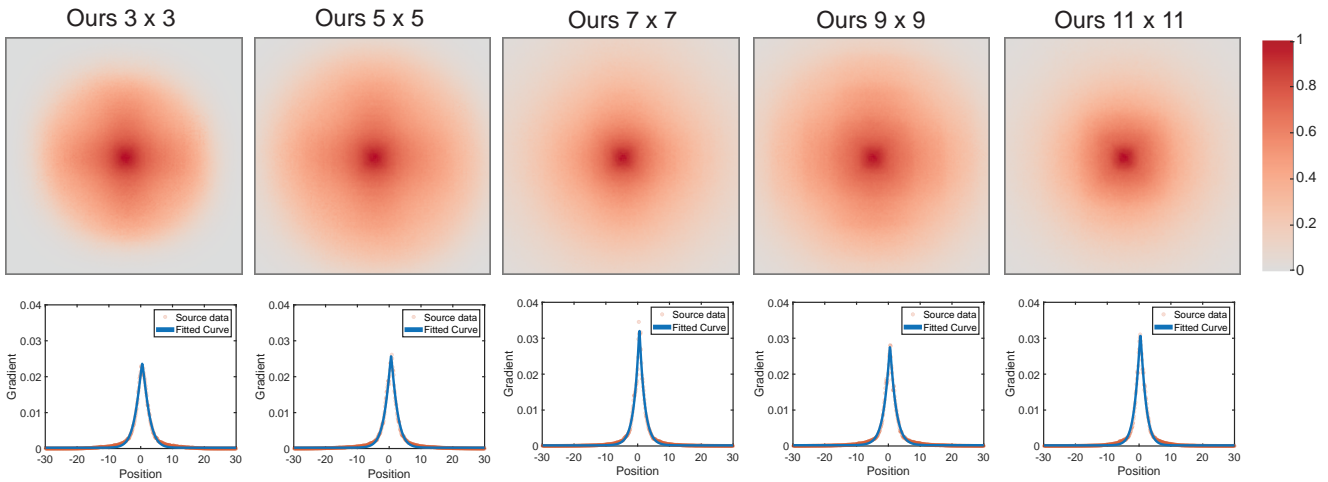
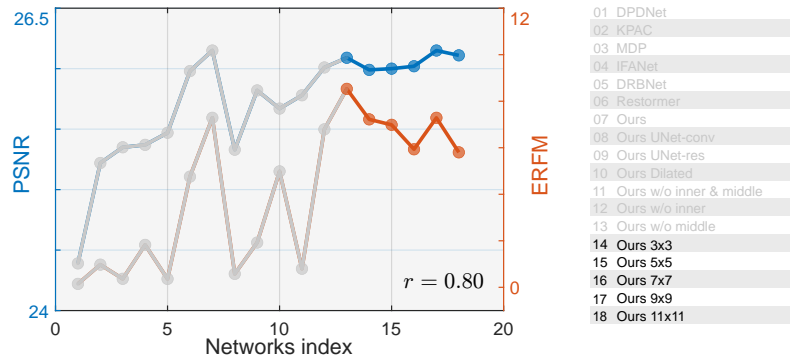


Figure 12. Demonstration of ERF patterns and the fitted GND-PDF curves: Here, we consider our network with different kernel sizes.

Table 16. ERF fitting parameters and statistics for our network with different kernel sizes.

Method	Layer Name	σ	β	μ	c_1	c_2 (e-5)	R^2	PSNR	ERFM
ours (3 × 3)	bt_neck	2.3390	1.2508	0.4832	0.1032	23.31	0.9928	25.99	7.2201
ours (5 × 5)	bt_neck	2.0966	1.1722	0.5941	0.1024	24.59	0.9912	26.00	6.9847
ours (7 × 7)	bt_neck	1.6297	1.0267	0.5398	0.1071	16.86	0.9863	26.02	5.9340
ours (9 × 9)	bt_neck	1.9138	1.0812	0.5105	0.1044	21.27	0.9914	26.15	7.2870
ours (11 × 11)	bt_neck	1.7744	1.1446	0.4124	0.1067	17.42	0.9924	26.11	5.8027

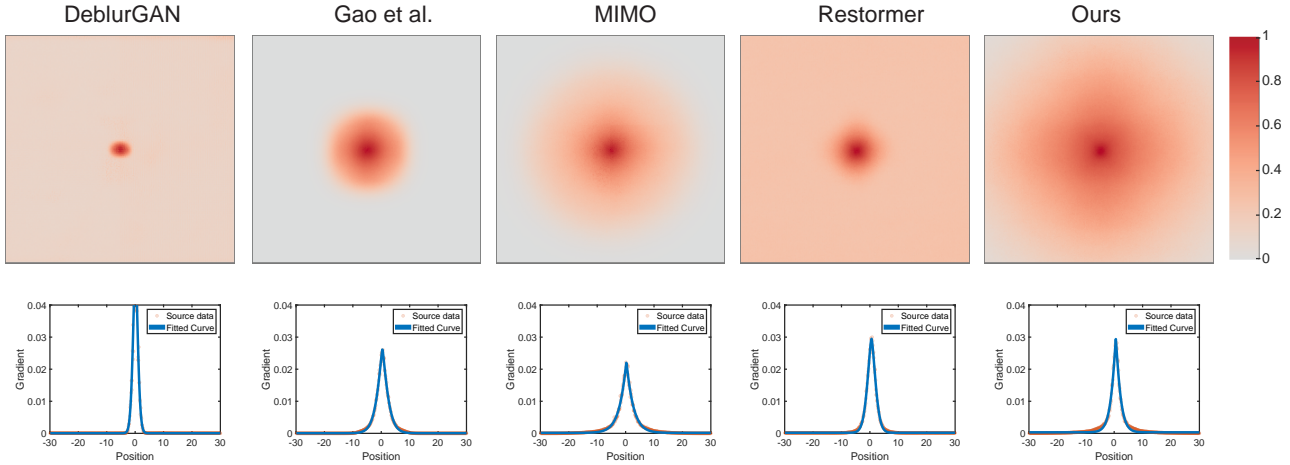


Figure 13. Demonstration of ERF patterns and the fitted GND-PDF curves: Here, different motion deblurring networks are considered.

Table 17. ERF fitting parameters and statistics for motion deblurring networks.

Method	Layer Name	σ	β	μ	c_1	c_2 (e-5)	R^2	PSNR	ERFM
DeblurGAN [30]	ResnetBlock_18	1.1834	1.6237	0.0865	0.1145	4.44	0.9563	28.70	2.4235
Gao <i>et al.</i> [21]	level3_deconv3_1	2.2912	1.2337	0.4046	0.1142	5.00	0.9967	30.90	5.3920
MIMO-UNet+ [11]	DB3	2.4514	1.0489	0.2753	0.1077	15.78	0.9902	32.45	5.3514
Restormer [84]	latent	1.9640	1.5154	0.5592	0.1054	19.63	0.9952	32.92	3.8813
Ours	bt_neck	1.7278	1.1311	0.5805	0.0977	32.52	0.9863	33.35	6.3704

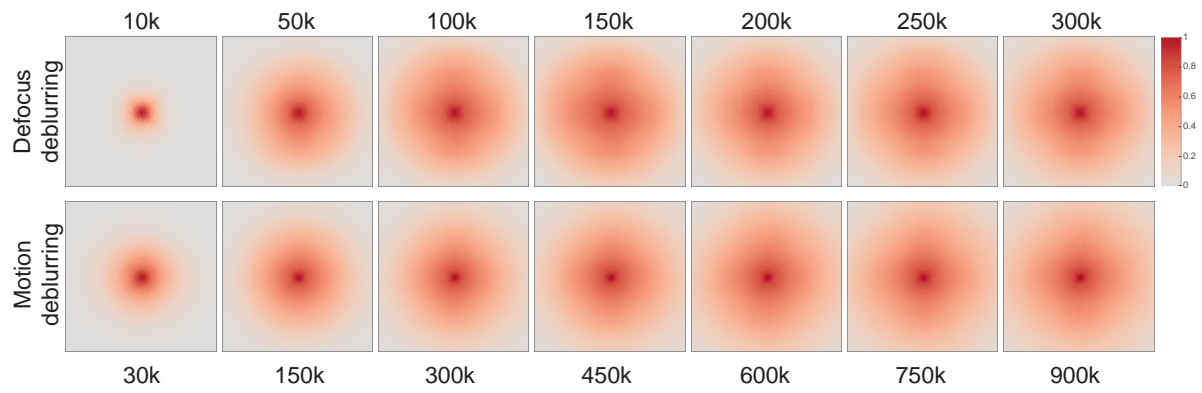


Figure 14. ERF evolution for increasing number of training cycles (from left to right) on defocus deblurring (up) and motion deblurring (down).

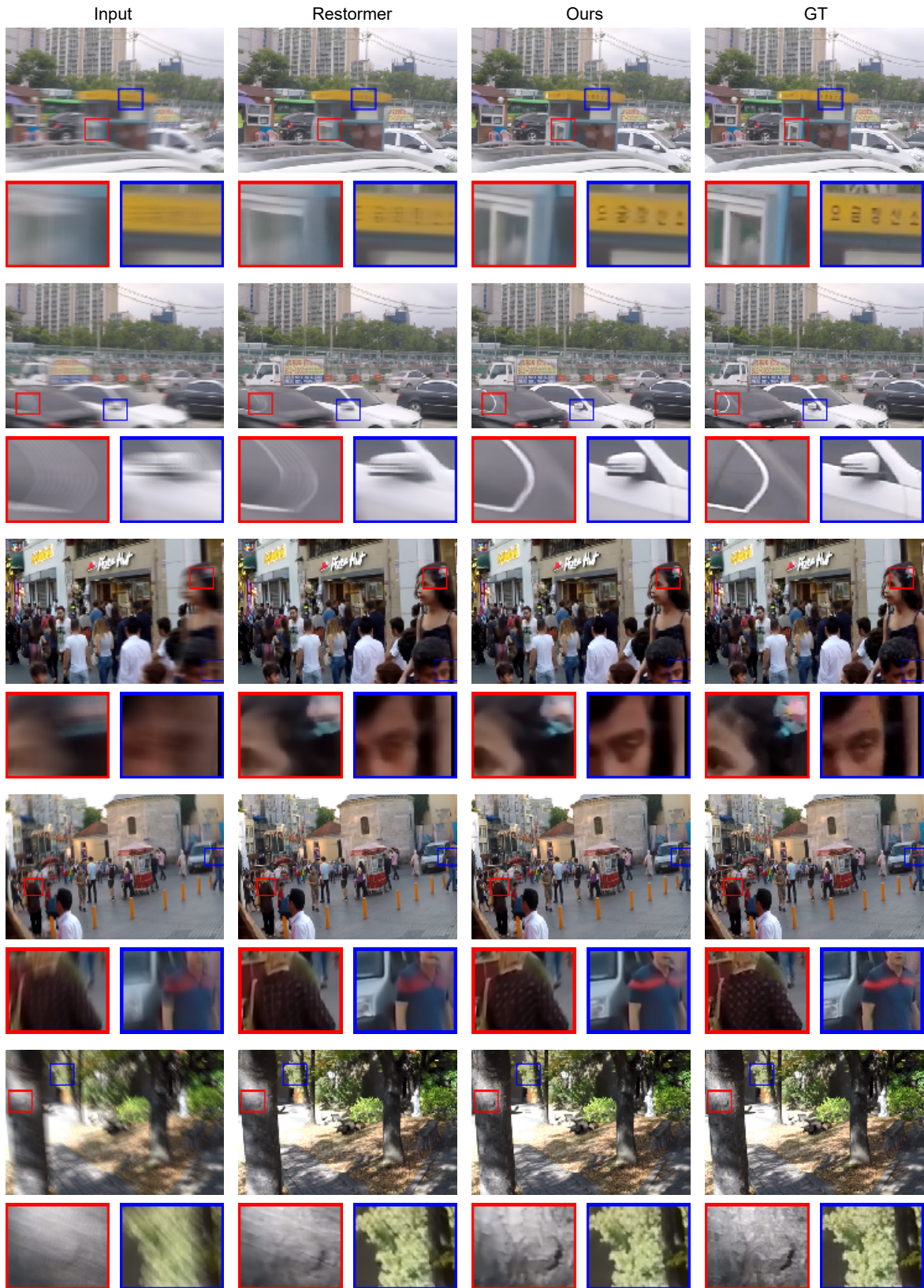


Figure 15. Qualitative comparison between Restormer [84] and our method evaluated on GoPro dataset.

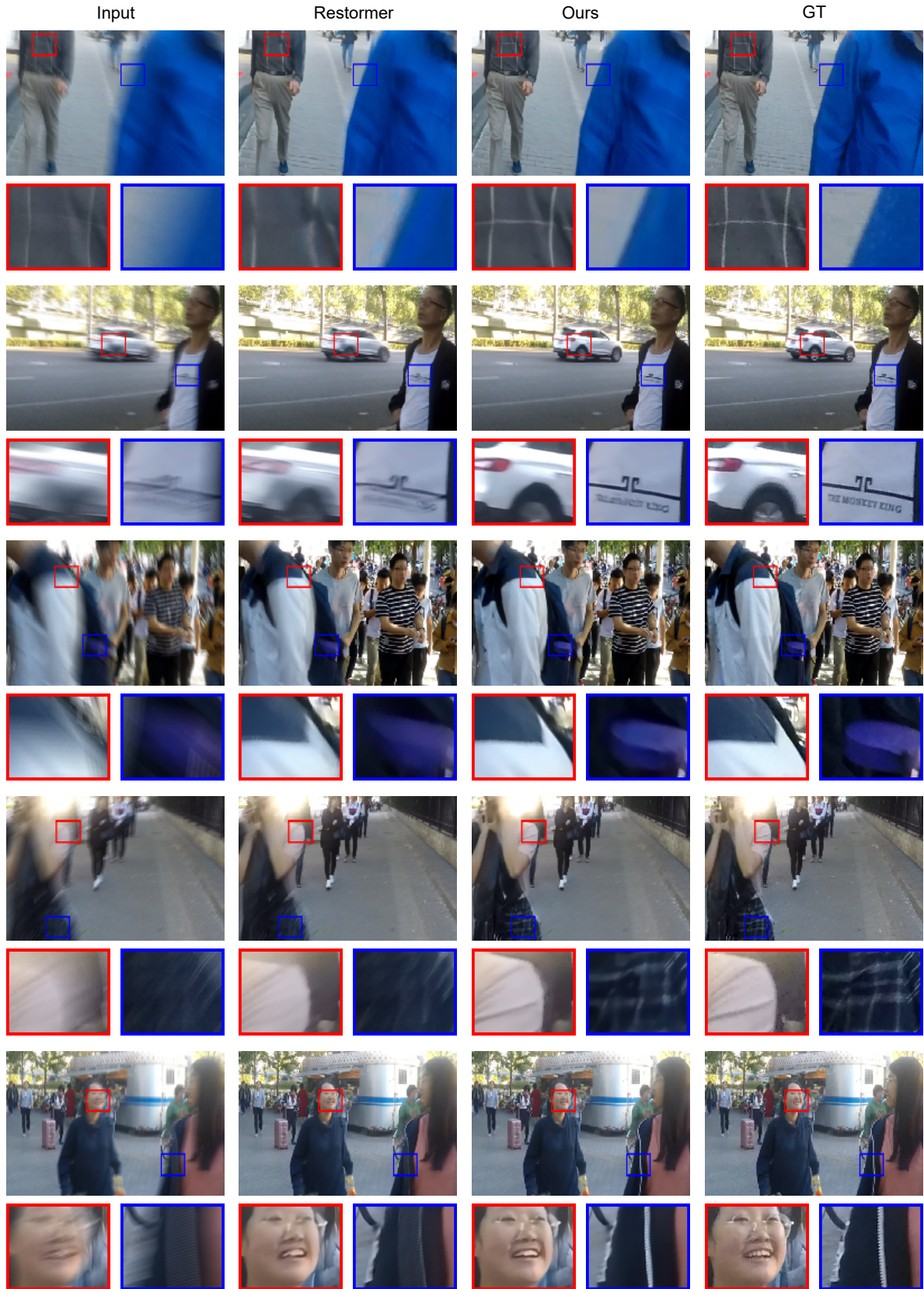


Figure 16. Qualitative comparison between Restormer [84] and our method evaluated on HIDE dataset.

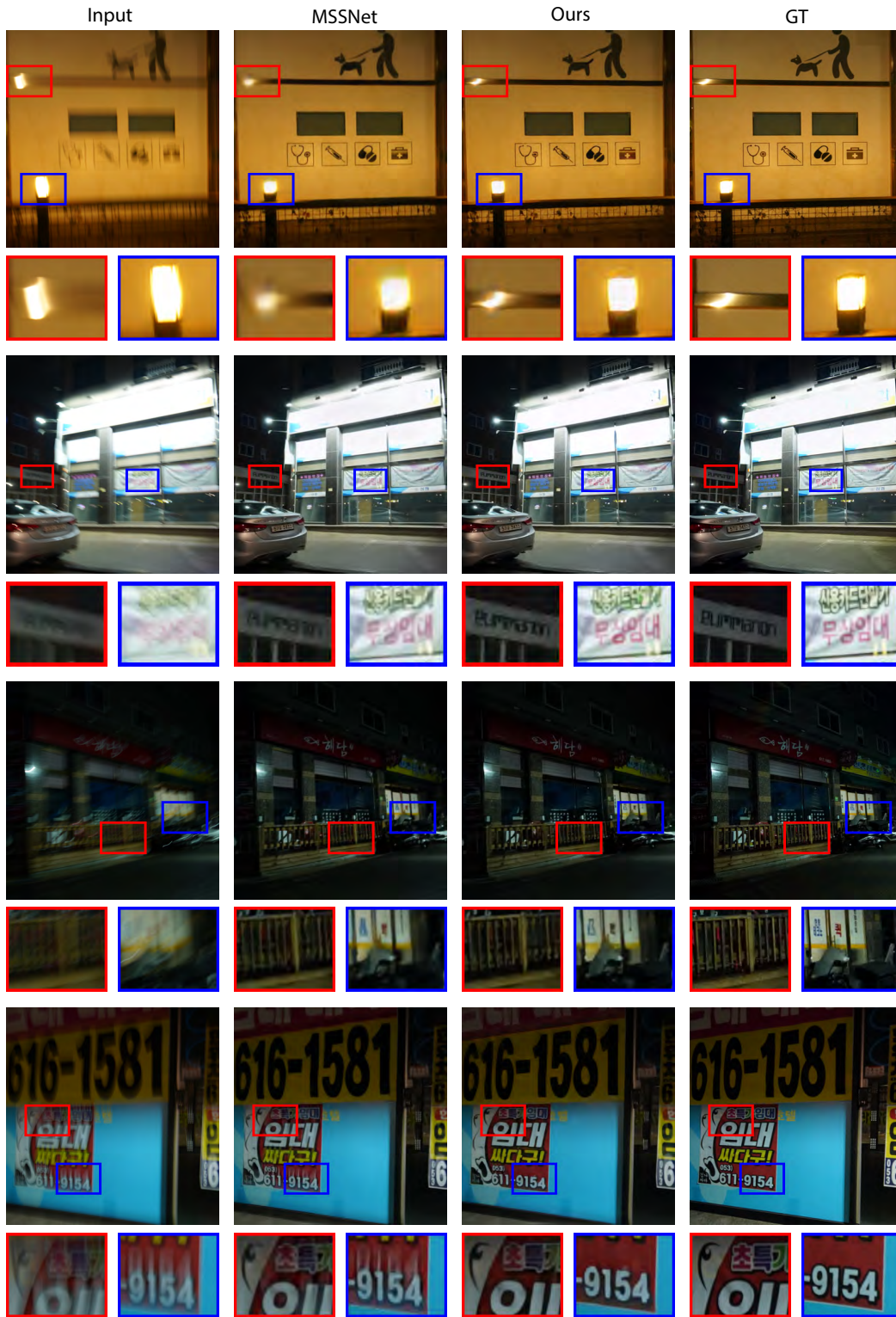


Figure 17. Qualitative comparison between MSSNet [28] and our method evaluated on RealBlur-J dataset.

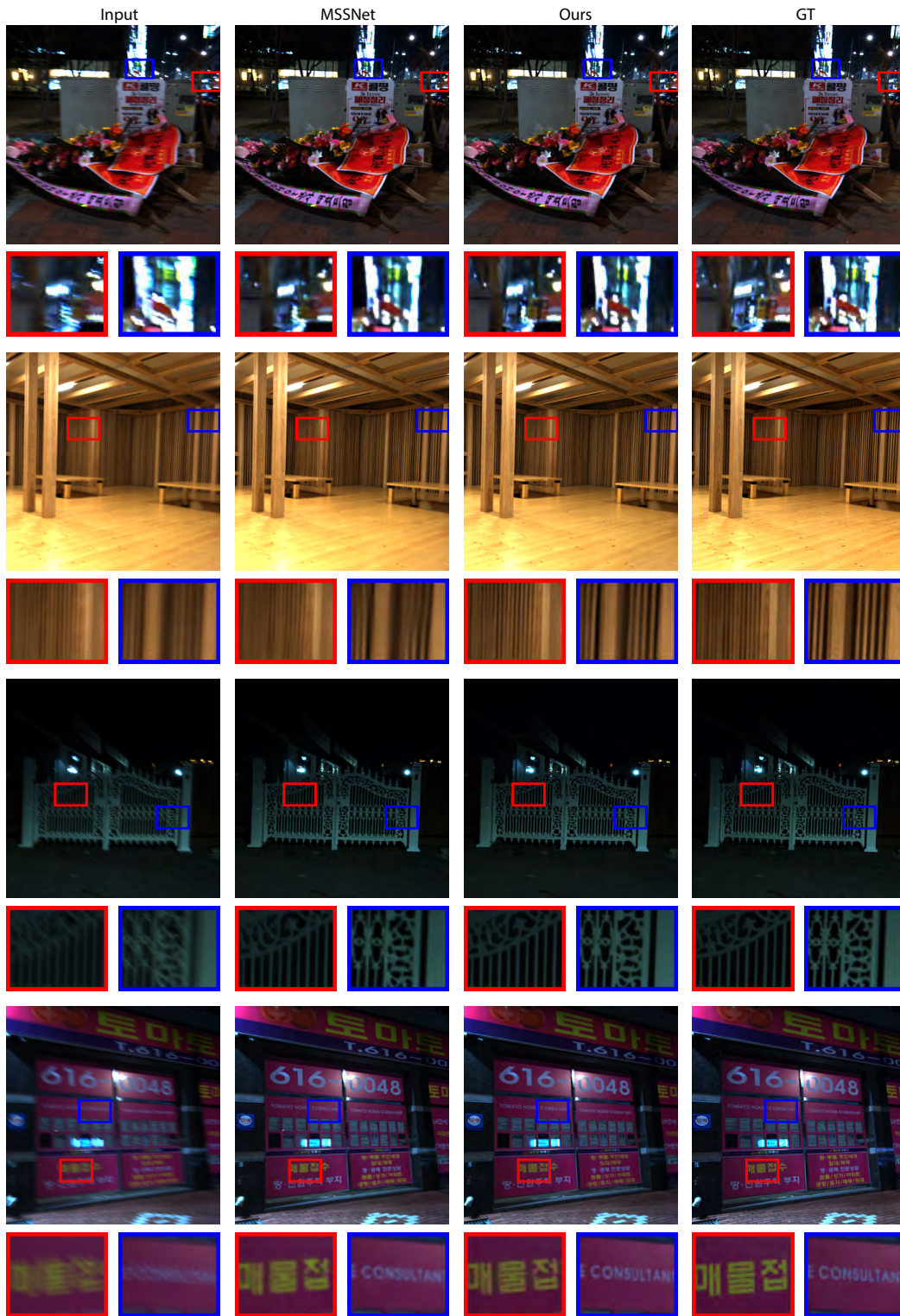


Figure 18. Qualitative comparison between MSSNet [28] and our method evaluated on RealBlur-R dataset.

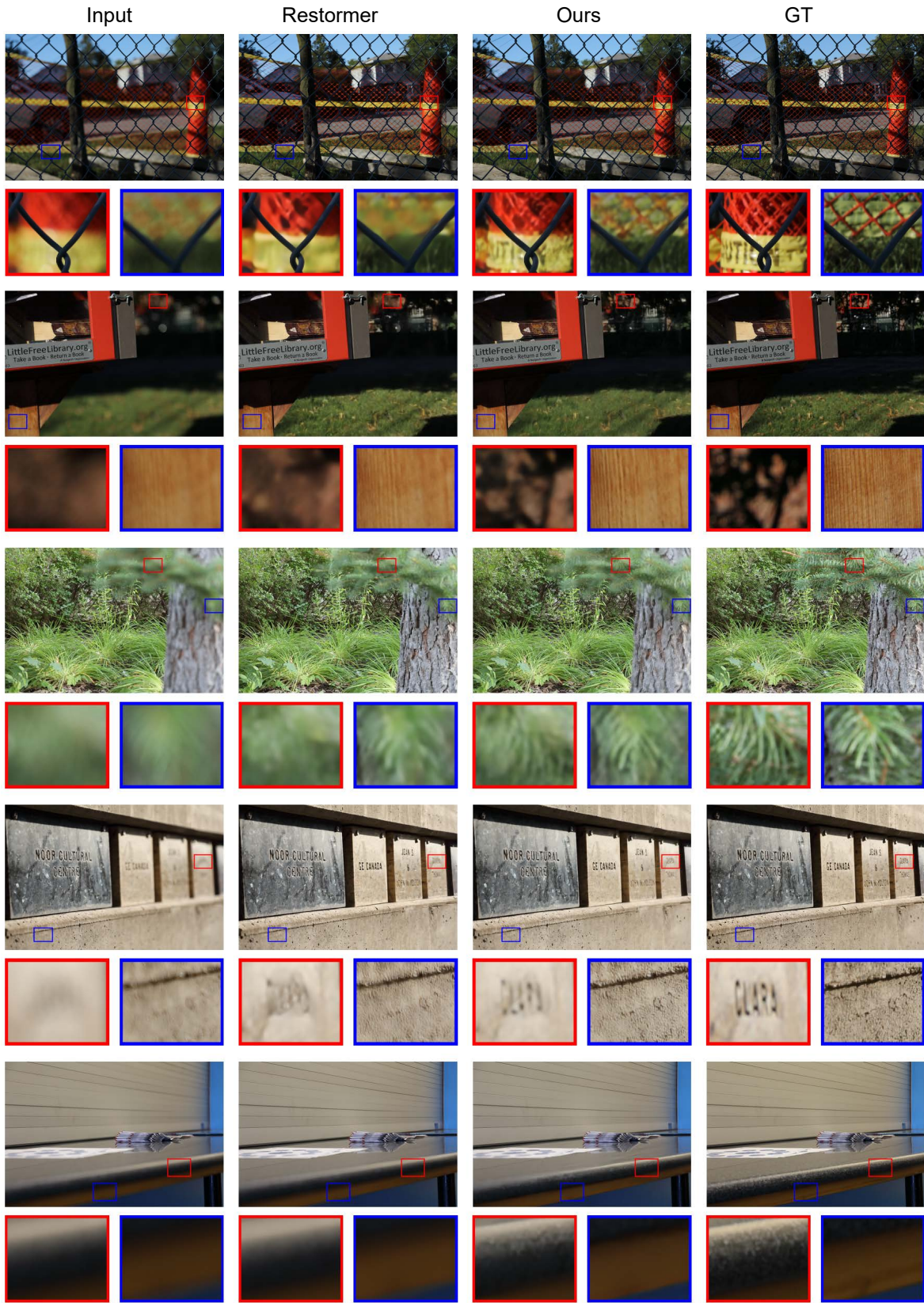


Figure 19. Qualitative comparison between Restormer [84] and our method evaluated on DPDD dataset.

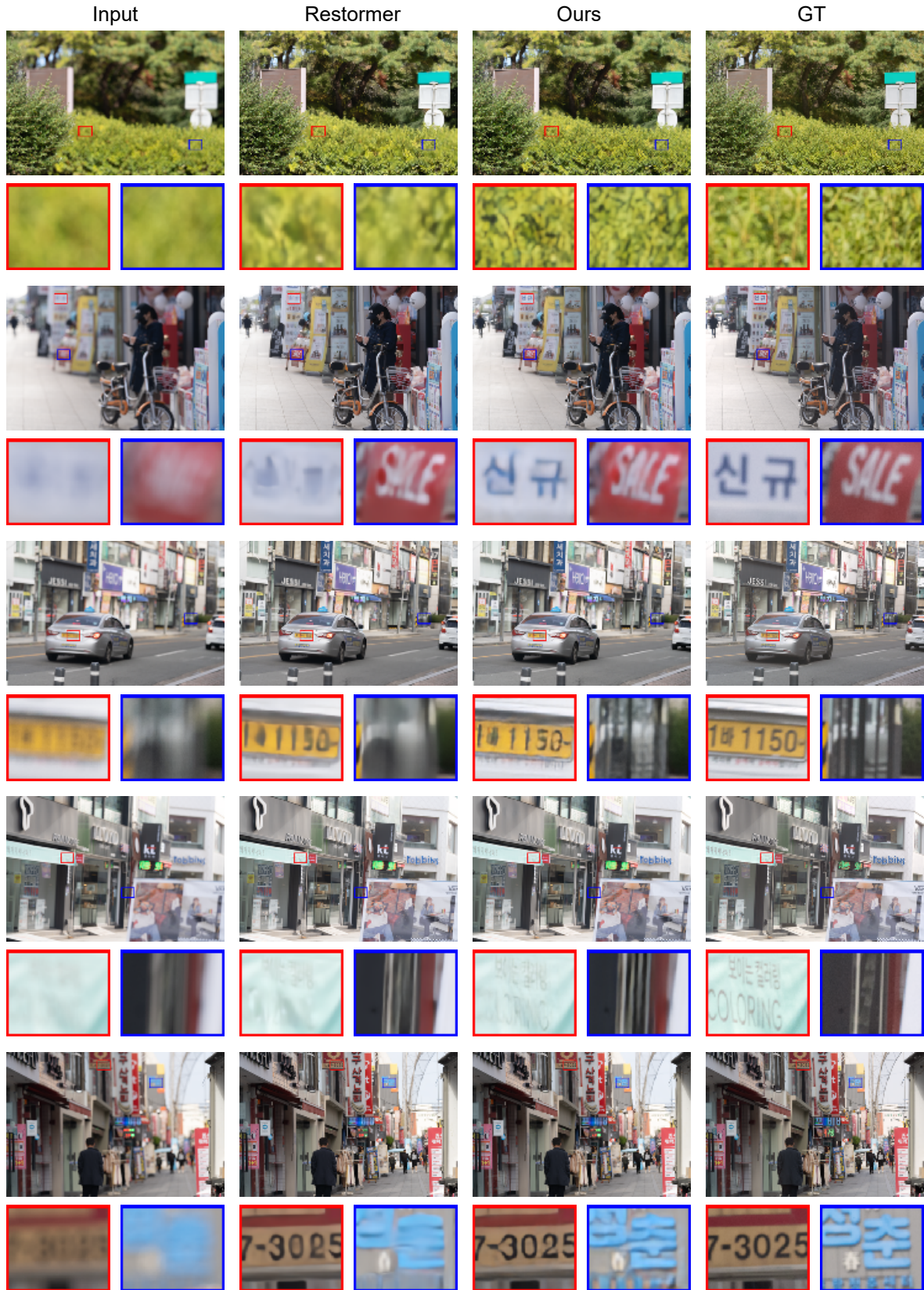


Figure 20. Qualitative comparison between Restormer [84] and our method evaluated on RealDOF dataset.

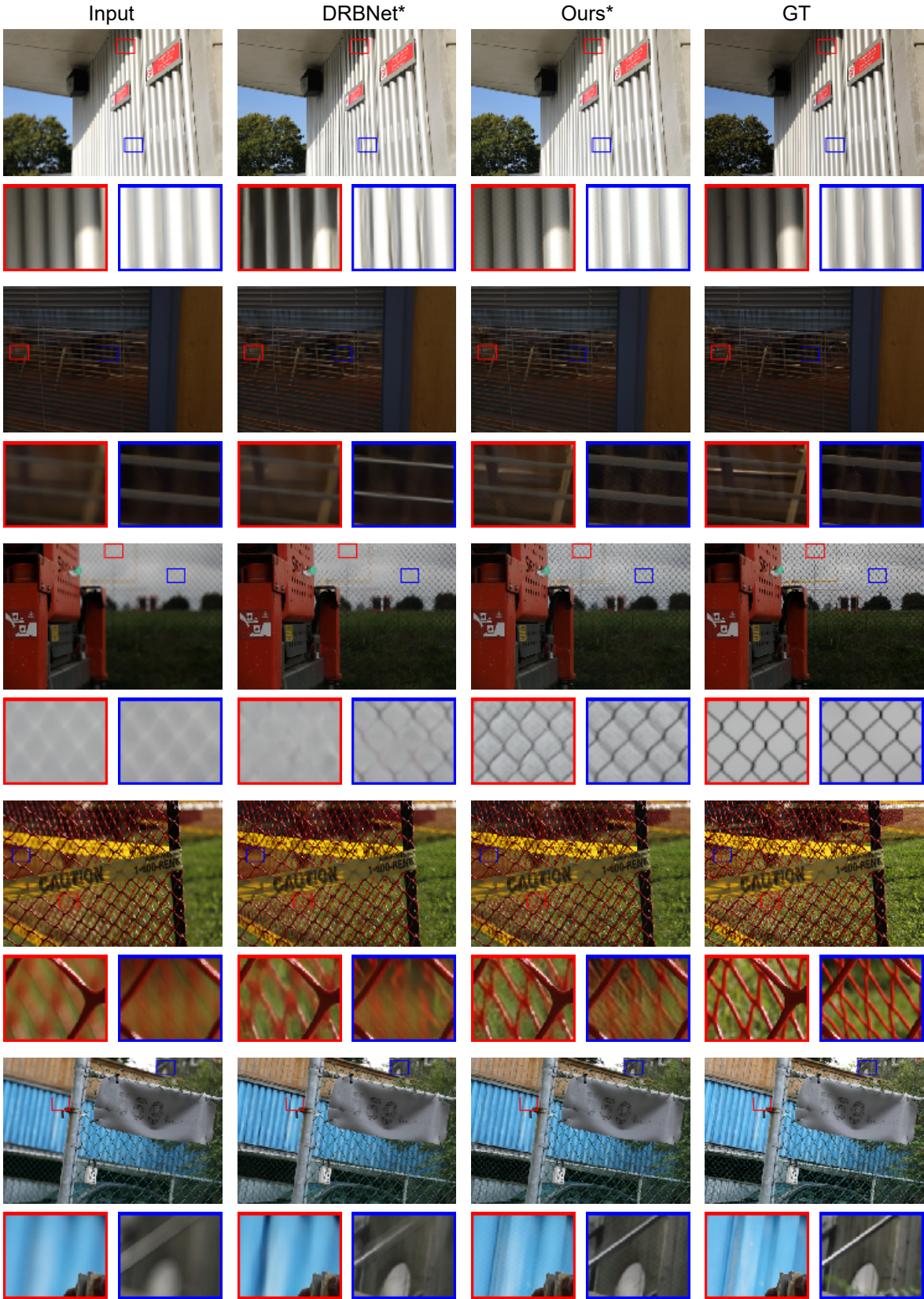


Figure 21. Qualitative comparison between DRBNet [53] and our method adopting the two-stage training strategy as proposed in [53] when evaluated on the DPDD dataset.

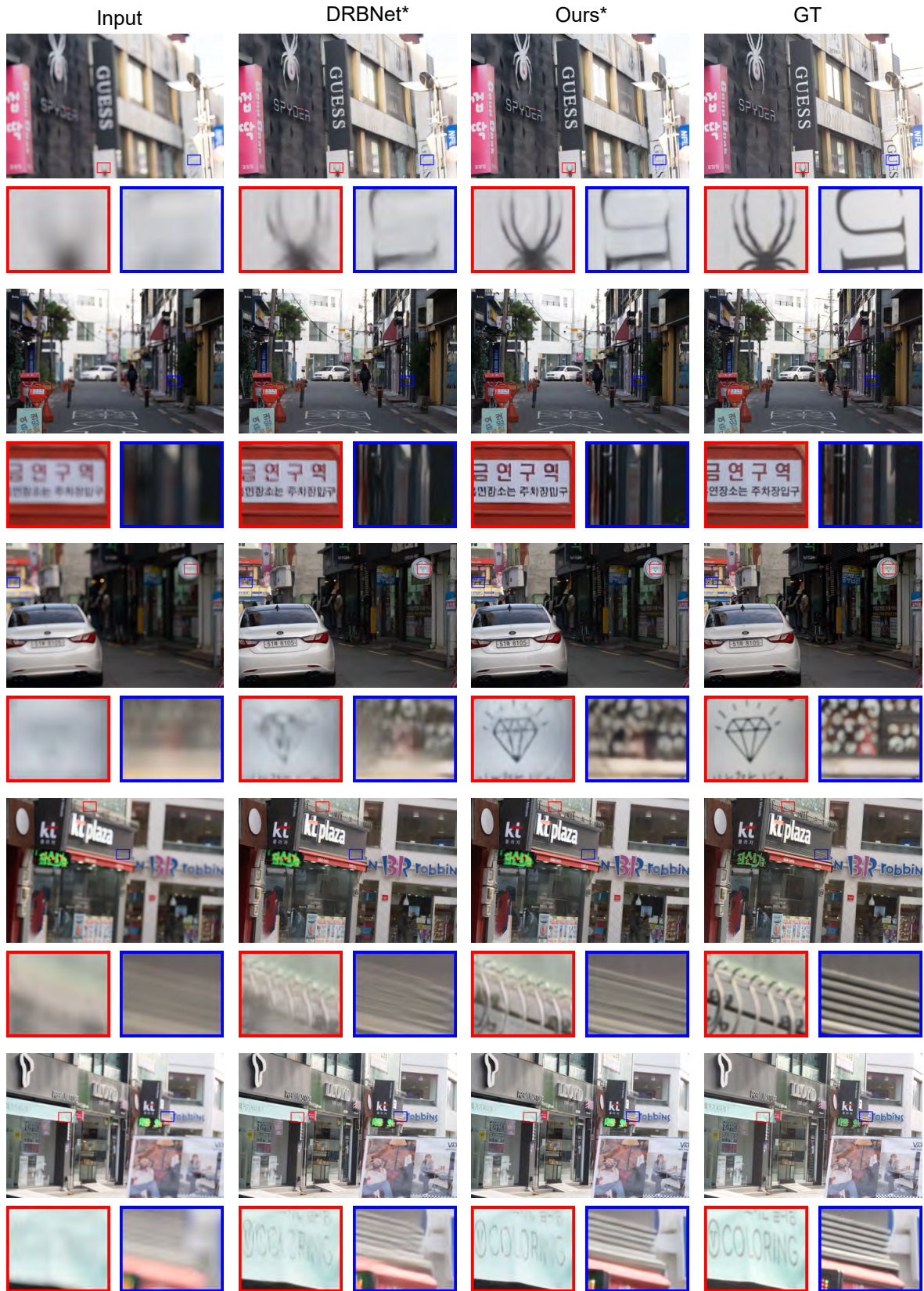


Figure 22. Qualitative comparison between DRBNet [53] and our method adopting the two-stage training strategy as proposed in [53] when evaluated on RealDOF dataset.

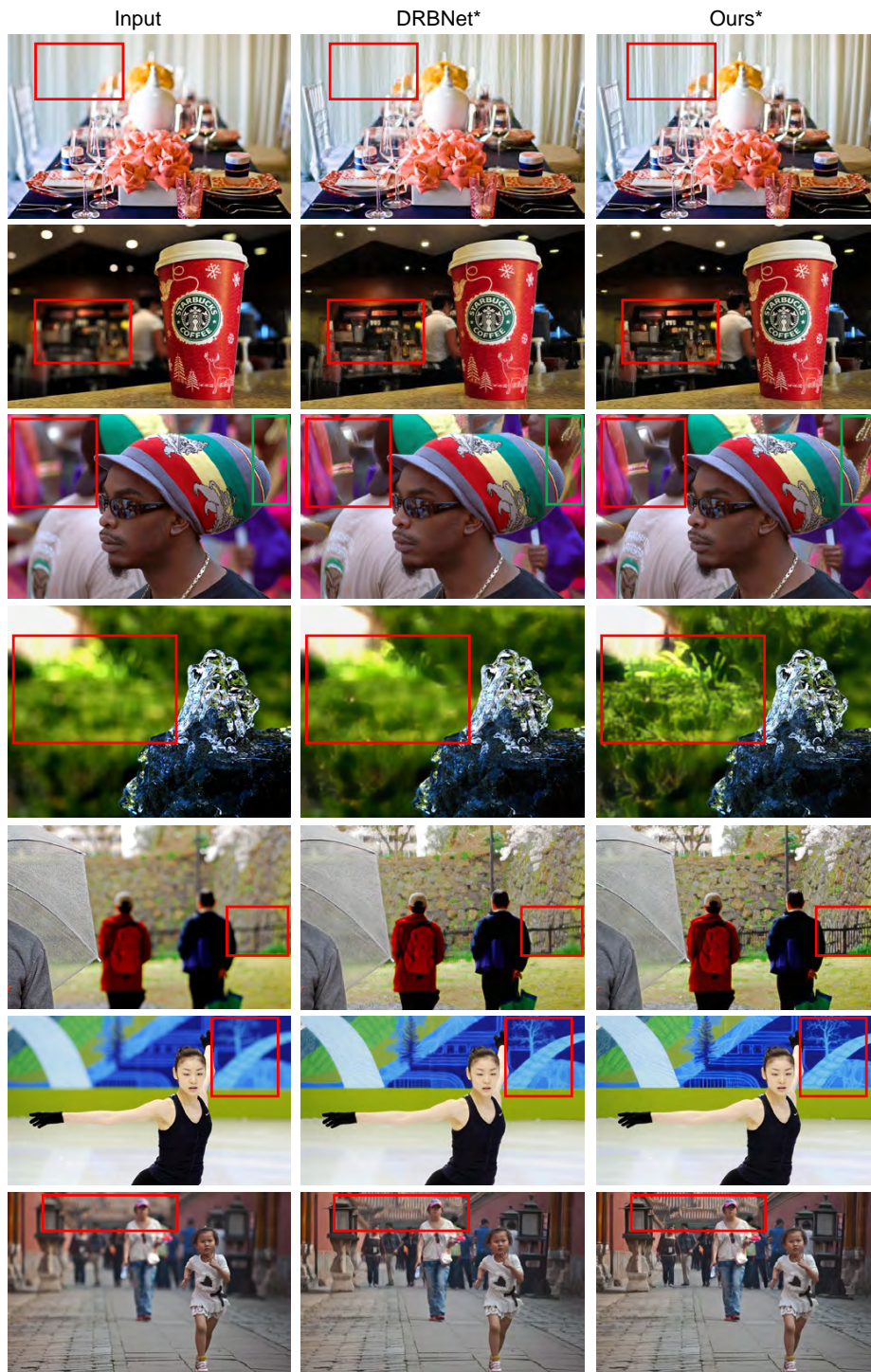


Figure 23. Qualitative comparison between DRBNet [53] and our method evaluated on CUHK dataset when adopting the training strategy proposed in [53]. Note no all-in-focus ground truth in CUHK dataset.

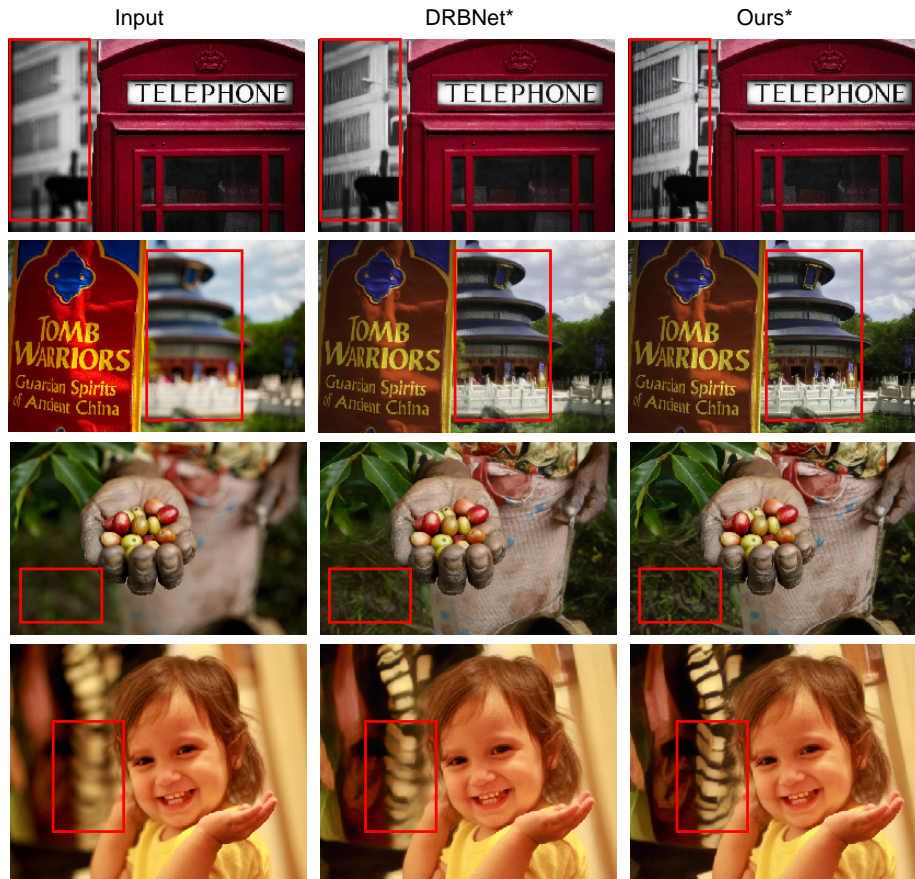


Figure 24. Qualitative comparison between DRBNet [53] and our method evaluated on CUHK dataset when adopting the training strategy proposed in [53]. Note no all-in-focus ground truth in the CUHK dataset.

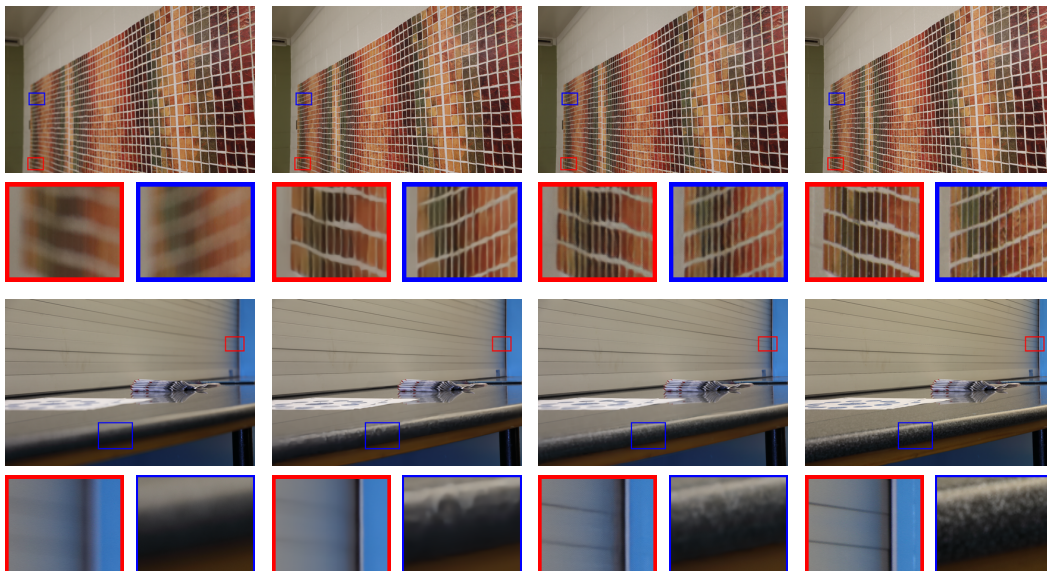


Figure 25. Dual-pixel defocus deblurring: Qualitative comparison between Restormer [84] and our method evaluated on DPDD dataset.